Properties of five $z \sim 0.3$–0.4 confirmed LyC leakers: VLT/XShooter observations

N. G. Guseva,[1][*] Y. I. Izotov,[1] D. Schaerer,[2,3] J. M. Vílchez [ID],[4] R. Amorín,[5,6] E. Pérez-Montero,[4] J. Iglesias-Páramo,[4,7] A. Verhamme,[2] C. Kehrig[4] and L. Ramambason[8]

[1]*Bogolyubov Institute for Theoretical Physics, Ukrainian National Academy of Sciences, Metrologichna 14b, Kyiv 03143, Ukraine*
[2]*Observatoire de Genève, Université de Genève, 51 Ch. des Maillettes, CH-1290 Versoix, Switzerland*
[3]*IRAP/CNRS, 14 Av. E. Belin, F-31400 Toulouse, France*
[4]*Instituto de Astrofísica de Andalucía – CSIC, Glorieta de la Astronomía s/n, E-18008 Granada, Spain*
[5]*Instituto de Investigación Multidisciplinar en Ciencia y Tecnología, Universidad de La Serena, Raúl Bitrán 1305, La Serena, Chile*
[6]*Departamento de Astronomía, Universidad de La Serena, Av. Juan Cisternas 1200 Norte, La Serena, Chile*
[7]*Estación Experimental de Zonas Áridas – CSIC, Ctra. de Sacramento s/n, E-04120 Almería, Spain*
[8]*Département d'Astrophysique, CEA, Université Paris-Saclay, F-91191 Gif-sur-Yvette, France*

ABSTRACT

Using new Very Large Telescope (VLT)/XShooter spectral observations we analyse the physical properties of five $z \sim 0.3$–0.4 confirmed Lyman continuum (LyC) leakers. Strong resonant Mg II $\lambda\lambda$2796, 2803 Å emission lines ($I(\lambda\lambda2796, 2803)/I(H\beta) \simeq$ 10–38 per cent) and non-resonant Fe II* $\lambda\lambda$2612, 2626 Å emission lines are observed in spectra of five and three galaxies, respectively. We find high electron densities $N_e \sim 400$ cm^{-3}, significantly higher than in typical low-z, but comparable to those measured in $z \sim 2$–3 star-forming galaxies (SFGs). The galaxies have a mean value of $\log$ N/O $= -1.16$, close to the maximum values found for SFGs in the metallicity range of $12 + \log$ O/H $\simeq 7.7$–8.1. All 11 low-z LyC emitting galaxies found by Izotov et al., including the ones considered in this study, are characterized by high equivalent width (EW) (Hβ) ~ 200–400 Å, high ionization parameter ($\log(U) = -2.5$ to -1.7), high average ionizing photon production efficiency $\xi = 10^{25.54}$ Hz erg^{-1}, and hard ionizing radiation. On the Baldwin–Phillips–Terlevich (BPT) diagram we find the same offset of our leakers from low-z main-sequence SFGs as that for local analogues of Lyman-break galaxies (LBGs) and extreme SFGs at $z \sim 2$–3. We confirm the effectiveness of the He I emission lines diagnostics proposed by Izotov et al. in searching for LyC leaker candidates and find that their intensity ratios correspond to those in a median with low neutral hydrogen column density $N(H I) = 10^{17}$–5×10^{17} cm^{-2} that permit leakage of LyC radiation, likely due to their density-bounded H II regions.

Key words: galaxies: abundances – galaxies: dwarf – galaxies: ISM – galaxies: starburst.

1 INTRODUCTION

Recently Izotov et al. (2016a,b, 2018a,b) have discovered significant emission of Lyman continuum (LyC) ionizing radiation leaking with the escape fractions of 2–76 per cent in a sample of 11 low-z compact active star-forming galaxies (SFGs) observed with the *Hubble Space Telescope* (*HST*) in conjunction with the Cosmic Origins Spectrograph (COS). These galaxies hereafter referred to as LyC leakers, possess many properties similar to those of high-redshift galaxies both at $z \sim 2$–3 and $z \gtrsim 6$ such as compact morphology with similar galaxy radii (e.g. Bouwens et al. 2004; Ferguson et al. 2004; Oesch et al. 2010; Ono et al. 2012; Shibuya, Ouchi & Harikane 2015; Curtis-Lake et al. 2016; Paulino-Afonso, Sobral & Ribeiro 2018), strong emission lines with high equivalent widths (EWs; e.g. Schaerer & de Barros 2009; Smit et al. 2014, 2015; Roberts-Borsani et al. 2016; Bowler et al. 2017; Castellano et al. 2017; Fletcher et al. 2019; Bian & Fan 2020; Endsley et al. 2020), similar low

stellar masses, low metallicities, and high specific star formation rates (SFRs; e.g. Jaskot & Oey 2013; Nakajima et al. 2013; Stark et al. 2013a; de Barros, Schaerer & Stark 2014; Duncan et al. 2014; González et al. 2014; Nakajima & Ouchi 2014; Becker, Bolton & Lidz 2015; Grazian et al. 2015; Salmon et al. 2015; Huang et al. 2016; Stark 2016; Santini et al. 2017; Stark et al. 2017; Dors et al. 2018), small dust content (e.g. Ouchi et al. 2013; Ota et al. 2014; Maiolino et al. 2015; Schaerer et al. 2015; Watson et al. 2015), and are considered as the main sources of reionization of the Universe after the cosmic 'Dark Ages'. This makes low-z LyC leakers the best local analogues of reionization galaxies (see e.g. Schaerer et al. 2016; Stark 2016; Ma et al. 2020). Given their proximity, these galaxies represent excellent laboratories for a detailed study of their physical conditions, and the main mechanisms responsible for LyC leakage. Ground-based spectroscopic observations in the visible and near-infrared ranges are necessary for that.

In this paper, we present a spectroscopic study with the European Southern Observatory (ESO) Very Large Telescope (VLT) in conjunction with the XShooter spectrograph of five LyC leaking galaxies from the Izotov et al. (2016a,b, 2018a,b) sample with LyC

[*] E-mail: nguseva@bitp.kiev.ua

Table 1. General characteristics of our sample galaxies.

Galaxy	RA (J2000)	Dec. (J2000)	z	$f_{esc}(LyC)^a$	$\log t^{\,b}$	$\log M_\star^{\,c}$	SFR^d	$EW(H\beta)^e$	$12 + \log O/H^f$	Detection^g
J0901+2119	09:01:45.61	+21:19:27.78	0.2993	2.7	2.4	9.80	20	357.5	8.05	Fe II*
J0925+1403	09:25:32.37	+14:03:13.06	0.3010	7.8	2.6	8.91	52	208.1	8.12	Fe II*
J1011+1947	10:11:38:28	+19:47:20.94	0.3322	11.4	3.4	9.00	24	314.9	7.97	...
J1154+2443	11:54:48.85	+24:43:33.03	0.3690	46.0	2.6	8.20	19	255.1	7.75	...
J1442−0209	14:42:31.39	−02:09:52.03	0.2937	7.3	3.4	8.96	36	186.8	7.98	Fe II*

$^{a\,-d}$Data obtained by Izotov et al. (2016a,b, 2018a,b).
^{a}Lyman continuum escape fraction in per cent.
^{b}Starburst age in Myr. Ages and stellar masses are derived from spectral energy distribution (SED) fitting of the Sloan Digital Sky Survey (SDSS) spectra.
$^c\,M_\star$ is the galaxy stellar mass in units of $M_\odot$.
^{d}Star formation rate obtained from the $H\beta$ luminosity according to Kennicutt (1998) in units of $M_\odot$ yr^{-1}.
^{e,f}Data obtained in this paper.
^{e}Equivalent width of $H\beta$ in Å.
^{g}Detection of Fe II* emission.

Table 2. Log of observations.

Name	Date	Exposure time^a			Airmass^b	Seeing^c	Spectrophotometric standard stars^d
		UVB	VIS	NIR			
J0901+2119	2019-01-09	8280	8640	1500	1.47	0.77	GD 71(1.69)
J0925+1403	2019-01-15	2760	2880	496	1.45	0.89	GD 71(1.69)
J1011+1947	2019-01-09	5520	5760	1000	1.40	0.93	GD 71(1.69), LTT 3218(1.36)
J1154+2443	2019-04-30	8280	8640	1500	1.54	1.10	EG 274(1.34), LTT 3218(1.38), LTT 7987(1.02)
J1442−0209	2019-05-24	2760	2880	500	1.08	0.99	LTT 3218(1.08)

^{a}In seconds.
^{b}Average airmass during observation.
^{c}Average seeing (full width at half-maximum, FWHM) in arcsec.
^{d}Spectrophotometric standard stars used for the flux calibration. They were observed at average airmasses shown in parentheses.

escape fractions $f_{esc}(LyC)$ = 2.7–46.0 per cent and low enough declinations ($<+25°$), making them accessible for observations at Paranal. Throughout of the text $f_{esc}(LyC)$ is the absolute escape fraction, which is defined as a ratio of the observed LyC flux corrected for Milky Way (MW) extinction, and the intrinsic galaxy LyC flux. Such observations provide an excellent opportunity for a comprehensive study of selected galaxies over a wide wavelength range ($\sim\lambda3000$–24000 Å). The basic properties of our galaxy sample are summarized in Table 1.

This paper is organized as follows. In Section 2, we describe the VLT/XShooter spectrophotometric observations and data reductions. In Section 3, we present the results obtained with the new observations. The element abundance determination with emphasizing the problems of nitrogen abundance is given in Section 3.1. High intensities of nebular helium emission line He II λ4686 Å are considered in Section 3.2. In Section 3.3, we discuss resonant Mg II $\lambda\lambda$2796, 2803 Å emission lines. The position of confirmed local LyC leakers on the Baldwin–Phillips–Terlevich (BPT) diagram and their ionization parameters and ionizing photon production efficiencies are discussed in Section 3.4. In Section 3.5, we present the He I emission line diagnostics for the LyC leakers. Finally, in Section 4, we summarize our main results.

2 OBSERVATIONS AND DATA REDUCTION

Spectral observations of five confirmed LyC leakers were carried out with the XShooter spectrograph mounted at the UT2 Cassegrain focus of the VLT in nodding-on-slit mode during 2019 (ESO Program ID 0102.B-0942(A)). The use of three UVB (1 × 11 arcsec^2 slit, $R \approx 5100$), VIS (0.9 × 11 arcsec^2 slit, $R \approx 8800$), and NIR (0.9 × 11 arcsec^2 slit, $R \approx 5100$) arms made it possible to obtain the spectrum of each object simultaneously over a wide wavelength range, in particular in the UVB, VIS, and NIR arms with wavelength ranges $\sim\lambda$3000–5600, $\sim\lambda$5500–10 200, and $\sim\lambda$10 200–24 000 Å, respectively. All observations were obtained during clear nights. We note that two galaxies J1011+1947 and J1154+2443 were observed during several nights. For the flux calibration, several standard stars (GD 71, LTT 3218, EG 274, LTT 7987) were observed at various airmasses in the range 1.02–1.69. The log of observations is presented in Table 2.

IRAF[1] was used to reduce the observations and, as the first step, to subtract the bias in the UVB and VIS arms and dark frames in the NIR arm. Applying the CRMEDIAN routine to all UVB, VIS, and NIR arms, we removed the cosmic rays. We applied the correction for telluric absorption of the galaxy spectra in the wavelength ranges that include [S II] λ6717, 6731 emission lines. To do this we produce the normalized spectrum of the standard star from its observed spectrum, i.e. adopting its continuum equal to unity. Then the spectrum of the galaxy corrected for telluric absorption is derived dividing the observed galaxy spectrum by the normalized standard star spectrum. However, no correction has been done for [S III] λ9069, 9531 emission lines because of stronger and variable telluric bands of H_2O. The correction for the pixel sensitivity, background subtraction, wavelength calibration, and correction for distortion and tilt of each frame were performed. After this, the one-dimensional spectra were extracted from the two-dimensional frames in apertures of 1.6 arcsec along the slit for UVB and VIS arms and 2.4 arcsec for NIR arm. The flux-calibrated rest-frame spectra are shown in Fig. A1.

---

[1] IRAF is distributed by the National Optical Astronomy Observatories, which are operated by the Association of Universities for Research in Astronomy, Inc., under cooperative agreement with the National Science Foundation.

Emission line fluxes and their errors were measured in flux-calibrated and non-flux-calibrated spectra, respectively, using total integral fluxes with the IRAF SPLOT routine (see for more details, e.g. Guseva et al. [2012](#), [2015](#); Izotov, Thuan & Guseva [2014a](#)). The internal extinction and underlying hydrogen stellar absorption were derived iteratively from the Balmer decrement following Izotov, Thuan & Lipovetsky ([1994](#)) and adopting the Cardelli, Clayton & Mathis ([1989](#)) reddening law with $R(V) = 3.1$, after correcting the spectra for MW extinction. The MW extinction correction was applied to the spectrum at observed wavelengths adopting the extinction $A(V)$ from the NASA/IPAC Extragalactic Database (NED) and the same value of $R(V)$. It was also assumed that EWs of absorption lines are the same for all hydrogen Balmer transitions. The EWs of the Balmer absorption lines range from 2.5 to 3.5 Å, compatible with the predictions of the evolutionary stellar population synthesis models by González-Delgado, Leitherer & Heckman ([1999](#)) for young starbursts.

Extinction-corrected fluxes $I(\lambda)$ relative to Hβ multiplied by 100, EWs of emission lines, EW of underlying hydrogen absorption lines EW(abs), the extinction coefficient $C(H\beta)$, and the observed flux of Hβ for each galaxy are given in Table A1.

3 RESULTS

3.1 Physical properties and element abundances

To derive physical conditions and element abundances we follow prescriptions by Izotov et al. ([2006](#)) (see also e.g. Izotov & Thuan [2004](#); Izotov, Thuan & Guseva [2019](#)). Briefly, Izotov et al. ([2006](#)) adopt the three zone model of the H II region with respective electron temperatures $T_e(O\,III)$, $T_e(S\,III)$, and $T_e(O\,II)$. The electron temperature $T_e(O\,III)$ is derived from the ratio of [O III] line fluxes $\lambda 4363/\lambda(4959 + 5007)$ in the high-ionization zone. It is used to obtain abundances of ions O^{2+}, Ne^{2+}, and Ar^{3+}. Electron temperatures $T_e(O\,II)$ and $T_e(S\,III)$ are derived from relations obtained from photoionization models of H II regions. The electron temperature $T_e(S\,III)$ in the intermediate-ionization zone is used to derive the abundances of ions S^{2+} and Ar^{2+}. The electron temperature $T_e(O\,II)$ in the low-ionization zone is used to derive the abundances of ions O^+, N^+, S^+, Mg^+, and Fe^{2+}. The sulfur emission line ratio [S II] $\lambda 6717/\lambda 6731$ is used to derive the electron number density $N_e(S\,II)$. The total heavy element abundances are obtained with the use of ionization correction factors (ICFs) by Izotov et al. ([2006](#)).

For comparison we also provide the electron temperatures and electron number densities obtained with IRAF routine TEMDEN. Additionally we use equation (7) by Sanders et al. ([2016](#)) for electron number density determinations from the [O II] $\lambda 3729/\lambda 3726$ and [S II] $\lambda 6717/\lambda 6731$ line ratios with new collision strengths of Tayal ([2007](#)) for [O II] and Tayal & Zatsarinny ([2010](#)) for [S II] and with transition probabilities for both species of Fischer & Tachiev ([2014](#)). It is worth emphasizing that even small changes in flux ratios of components of [O II] doublet, as it is in the case of IRAF TEMDEN or method by Sanders et al. ([2016](#)), can result in large errors of the electron number density.

In the XShooter observations, the two components of [O II] are resolved but slightly blended, and the [S II] doublet often falls into the wavelength region of strong telluric absorption lines. For example, in the case of J1442–0209 the [S II] is shifted to the region of night sky O_2 band at rest-frame wavelengths $\lambda\lambda 8700$–8715 Å. [S II] lines in spectra of J1011+1947 and J1154+2443 are in the forest of telluric absorption lines as it is seen in the spectra of a standard star. $T_e(S\,III)$ cannot be determined from the XShooter spectra using the [S III] $\lambda 9069$ and $\lambda 9531$ lines, since these lines fall into the wavelength region of strong telluric absorption. The correction for the telluric absorption introduces uncertainties influencing the number density values in Table 3. Based on this, we calculated the ionic and element abundances using the method by Izotov et al. ([2006](#)), the values of $T_e(O\,III)$, $T_e(O\,II)$, and $T_e(S\,III)$ in the first three lines of Table 3 and $N_e(S\,II)$ in the sixth line of the same table with the exception of galaxies J1154+2443 and J1442–0209, for which N_e were taken from the [O II] $\lambda 3726$, 3729 doublet ratio adopting the average of highlighted values in Table 3. Electron temperatures $T_e(O\,III)$, $T_e(O\,II)$, and $T_e(S\,III)$, electron number densities $N_e(S\,II)$ and $N_e(O\,II)$, ionic abundances, ICFs, and element abundances of oxygen, nitrogen, neon, sulfur, argon, iron, and magnesium are given in Table 3.

Using most reliable determinations of N_e in high-z SFGs from Christensen et al. ([2012](#)), Stark et al. ([2013b](#)), James et al. ([2014](#)), Bayliss et al. ([2014](#)), Steidel et al. ([2014](#), [2016](#)), and Sanders et al. ([2020](#)) with element abundances derived by the direct T_e method and dividing them into groups by distance/redshift, we obtain average electron number densities $N_e \sim 260$ cm^{-3} ($z \sim 1.4$), $N_e \sim 460$ cm^{-3} ($z \sim 2.3$), and $N_e \sim 450$ cm^{-3} ($z \sim 3.5$). For our LyC leakers, the average $N_e(O\,II)$ is ~ 415 cm^{-3} and average $N_e(S\,II)$ excluding J1154+2443 and J1442–0209 is ~ 400 cm^{-3}. It follows from the above discussion that electron number densities in our LyC leakers are similar to the electron number densities in high-z galaxies and are considerably higher than $N_e(O\,II) = 30$ and 254 cm^{-3} (Harshan et al. [2020](#)) typical for local Sloan Digital Sky Survey (SDSS) Data Release 7 (DR7) SFGs and SFGs at $z \sim 1.5$, respectively.

The dependences of the Ne/O, S/O, Ar/O, Fe/O, and Mg/O ratios on oxygen abundance for our LyC leakers are similar to those for other samples of SFGs (e.g. HeBCD sample for the determination of helium abundances in blue compact dwarf galaxies by Izotov & Thuan [2004](#); Izotov et al. [2004](#)) and SFGs from SDSS Data Release 14 (DR14; Izotov et al. [2006](#); Guseva et al. [2011](#); Izotov, Guseva & Thuan [2011b](#); Izotov, Thuan & Guseva [2012](#)) with a similar spread of data (Fig. 1). Note that in this figure we only show SDSS DR14 SFGs with precise data, where element abundances are derived by the direct T_e method and the [O III] $\lambda 4363$ Å fluxes are measured with an accuracy better than 4σ.

3.1.1 Nitrogen abundance

The distribution of nitrogen to oxygen abundance ratio is a special case. It is seen in Fig. 1(a) that our LyC leakers occupy the upper part of the N/O spread with the mean value $\log N/O = -1.16$ that is ~ 0.3 dex lower than the solar value $\log (N/O)_\odot = -0.87$. We note that there are many other SFGs at oxygen abundances $12 + \log O/H \lesssim 8$ in Fig. 1(a) with an enhanced $\log N/O$, while the lowest $\log N/O$ for these oxygen abundances in SDSS and HeBCD samples attain values as low as ~ -1.7 to -1.6 (see also Amorin, Pérez-Montero & Vílchez [2010](#); Amorin, Vílchez & Pérez-Montero [2012b](#); Sanders et al. [2016](#); Vincenzo et al. [2016](#); Kojima et al. [2017](#)). This metallicity range is usually attributed to the primary N production. At higher $12 + \log O/H > 8$–8.5 both primary and secondary mechanisms may be responsible for the observed enhancement (Charlot & Longhetti [2001](#); Köppen & Hensler [2005](#); Mollá et al. [2006](#); Pilyugin, Grebel & Mattsson [2012](#); Andrews & Martini [2013](#)). In earlier data releases of the SDSS (e.g. Izotov et al. [2004](#); Amorin et al. [2010](#), [2012b](#)) only very few SFGs with $\log N/O > -1.4$ were found at $12 + \log O/H \lesssim 8$. Now we have collected more data in the SDSS DR14, resulting in much higher number of galaxies with large N/O at the low and

Table 3. Ionic and total heavy element abundances.

Property	Galaxy				
	J0901+2119	J0925+1403	J1011+1947	J1154+2443	J1442–0209
T_e(O III) (K)	13658 ± 232	12426 ± 227	15142 ± 285	16441 ± 505	14046 ± 278
T_e(O II) (K)	13144 ± 209	12200 ± 210	14080 ± 247	14720 ± 422	13410 ± 248
T_e(S III) (K)	12652 ± 193	12135 ± 188	13677 ± 237	15498 ± 419	12995 ± 231
T_e(O III)IRAF[a] (K)	13777 ± 320	12513 ± 306	15304 ± 396	16646 ± 663	14173 ± 378
T_e(O II)IRAF[a] (K)	13188 ± 662	13594 ± 681	...	...	11894 ± 622
N_e(S II) (cm^{-3})	364 ± 92	225 ± 76	608 ± 158	180 ± 150	88 ± 66
N_e(S II)IRAF[a] (cm^{-3})	387 ± 50	237 ± 42	652 ± 171	173 ± 209	80 ± 38
N_e(S II)new[b] (cm^{-3})	298 ± 39	194 ± 32	474 ± 114	146 ± 168	81 ± 35
N_e(O II)IRAF[a] (cm^{-3})	410 ± 14	296 ± 13	547 ± 35	**334 ± 30**	**341 ± 20**
N_e(O II)new[b] (cm^{-3})	481 ± 17	345 ± 15	646 ± 40	**365 ± 33**	**388 ± 24**
O^+/H^+ ($\times10^4$)	0.131 ± 0.007	0.205 ± 0.013	0.034 ± 0.002	0.048 ± 0.004	0.124 ± 0.008
O^{++}/H^+ ($\times10^4$)	0.976 ± 0.051	1.085 ± 0.063	0.890 ± 0.048	0.502 ± 0.040	0.833 ± 0.048
O^{+++}/H^+ ($\times10^6$)	0.896 ± 0.193	1.497 ± 0.237	1.528 ± 0.239	0.992 ± 0.241	1.017 ± 0.151
O/H ($\times10^4$)	1.116 ± 0.051	1.305 ± 0.064	0.939 ± 0.048	0.561 ± 0.040	0.967 ± 0.049
$12 + \log$(O/H)	8.048 ± 0.020	8.116 ± 0.021	7.973 ± 0.022	7.749 ± 0.031	7.985 ± 0.022
N^+/H^+ ($\times10^6$)	0.115 ± 0.005	0.135 ± 0.006	0.033 ± 0.002	0.038 ± 0.002	0.078 ± 0.003
ICF	7.617	5.932	2.668	0.402	7.103
$\log$(N/O)	-1.106 ± 0.028	-1.213 ± 0.029	-1.095 ± 0.033	-1.158 ± 0.045	-1.242 ± 0.030
Ne^{++}/H^+ ($\times10^5$)	1.962 ± 0.114	2.420 ± 0.159	1.273 ± 0.075	0.872 ± 0.072	1.752 ± 0.112
ICF	1.041	1.087	0.985	1.038	1.055
$\log$(Ne/O)	-0.738 ± 0.034	-0.696 ± 0.038	-0.874 ± 0.035	-0.792 ± 0.049	-0.719 ± 0.038
S^+/H^+ ($\times10^6$)	0.019 ± 0.001	0.025 ± 0.001	0.005 ± 0.000	0.008 ± 0.001	0.018 ± 0.001
S^{++}/H^+ ($\times10^6$)	0.118 ± 0.009	0.133 ± 0.011	0.067 ± 0.009	0.052 ± 0.009	0.106 ± 0.009
ICF	1.722	1.532	3.611	1.694	1.580
$\log$(S/O)	-1.675 ± 0.035	-1.731 ± 0.038	-1.555 ± 0.056	-1.739 ± 0.070	-1.693 ± 0.038
Ar^{++}/H^+ ($\times10^7$)	0.033 ± 0.001	0.034 ± 0.002	0.016 ± 0.001	0.013 ± 0.002	0.026 ± 0.001
Ar^{+++}/H^+ ($\times10^7$)	0.015 ± 0.003	0.015 ± 0.003	0.022 ± 0.002	0.023 ± 0.003	0.009 ± 0.002
ICF	1.229	1.133	2.114	1.428	1.215
$\log$(Ar/O)	-2.443 ± 0.050	-2.530 ± 0.053	-2.436 ± 0.060	-2.467 ± 0.126	-2.482 ± 0.045
Fe^{++}/H^+ ($\times10^6$)($\lambda4658$)	0.196 ± 0.035	0.372 ± 0.047	...	...	...
Fe^{++}/H^+ ($\times10^6$)($\lambda4988$)	0.222 ± 0.028	0.179 ± 0.025	...	...	...
ICF	10.779	8.158	...	...	...
$\log$(Fe/O) ($\lambda4658$)	-1.724 ± 0.079	-1.633 ± 0.059	...	...	...
[O/Fe] ($\lambda4658$)	0.304 ± 0.079	0.213 ± 0.059	...	...	...
$\log$(Fe/O) ($\lambda4988$)	-1.669 ± 0.058	-1.951 ± 0.065	...	...	...
[O/Fe] ($\lambda4988$)	0.249 ± 0.058	0.531 ± 0.065	...	...	...
Mg^+/H^+ ($\times10^6$)	0.271 ± 0.014	0.357 ± 0.022	0.084 ± 0.006	0.140 ± 0.011	0.414 ± 0.022
ICF	14.478	11.353	30.020	16.738	13.365
$\log$(Mg/O)	-1.454 ± 0.030	-1.508 ± 0.034	-1.570 ± 0.033	-1.379 ± 0.047	-1.243 ± 0.032

Note. For J1154+2443 and J1442–0209 most reliable values of electron number densities are in bold. [a]Values obtained with IRAF routine TEMDEN.
[b]Electron number density obtained from equation (7) of Sanders et al. (2016).

extremely low metallicity end (see also Sánchez-Almeida et al. 2016). This leads to a flatter dependence of N/O on the oxygen abundance. Similar enhancements of N/O are found in other our local LyC leakers (Izotov et al. 2016a,b, 2018a,b) and in high-z analogues of the galaxies during the epoch of reionization (EoR) at $z \sim 6$–10 [e.g. Lyman α emitters (LAEs) and Lyman-break galaxies (LBGs) at $z \sim 2$ of Sanders et al. 2016; Kojima et al. 2017].

Several mechanisms were proposed to explain this enhancement. For example, Amorin et al. (2010, 2012b) and Loaiza-Agudelo, Overzier & Heckman (2020) attribute the N/O increase to a recent inflow of the relatively low-metallicity gas that substantially lowers the oxygen abundance. Another mechanism was proposed by Izotov et al. (2006). They showed that the local N/O enhancement in dense

nitrogen-enriched ejecta from the winds of the evolved most massive stars (WR stars) can reach a factor of $\sim$20 during the first 4–5 Myr after onset of the star formation burst. Adopting the electron number density in the clumps 10 times higher than in the ambient H II region they estimated the apparent enhancement of N/O in compact SFGs to a factor of $\sim$2. Our leakers belong to low-metallicity, compact (exponential disc scale length $\alpha \sim 1$–1.5 kpc), low-mass ($M_\star \sim 10^8$–$10^9 M_\odot$), and relatively high-density galaxies with very young starbursts ($t \sim 3$–4 Myr), thus the local N/O enhancement may be very pronounced.

It is worth noting that no broad N III $\lambda4640$, He II $\lambda4686$, and C IV $\lambda5808$ emission lines are seen in the XShooter and SDSS spectra, likely due to the young age of star formation of the brightest burst
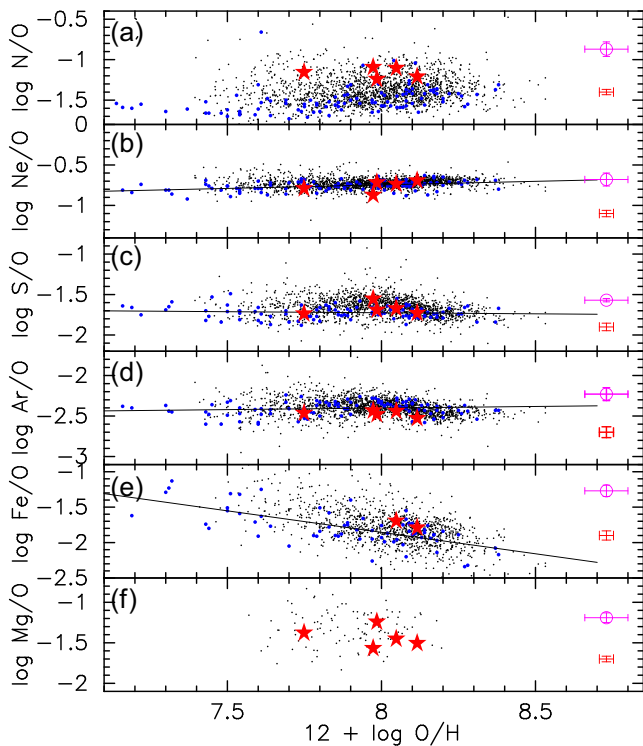
Figure 1. Dependences of different elemental abundance ratios X/O on the oxygen abundance 12 + log O/H for our sample shown by red stars. For comparison we show the HeBCD sample from Izotov & Thuan (2004) and Izotov et al. (2004) used for the primordial helium abundance determination (blue circles), and SFGs from the SDSS DR14 with the [O III]4363 Å fluxes measured with accuracy better than 4σ (black dots). Regressions to the reference data are presented by straight lines and solar values of Lodders (2020) are drawn by large magenta circles with error bars and averaged errors of LyC leakers by error bars in red.

and relatively low metallicity. Besides that the signal-to-noise (S/N) ratio in the continuum in the integral spectra of our LyC leakers is too low to detect very weak WR features.

Effects of differences in SFR and in star formation history of galaxies on the evolution of the relative abundance N/O during the long time period have been the subject of comprehensive studies (see e.g. Mollá et al. 2006). The position of our LyC leakers on the diagram N/O versus 12 + log O/H is similar to the position of SFGs from SDSS DR14 with high rate of star formation SFR > 20 M$_\odot$ yr^{-1} (Fig. 2c). Note that the ranges of SFR in the figure were chosen arbitrarily to emphasize the effect of SFR on the N/O ratio for a sample of SDSS DR14 SFGs. On the other hand, our leakers occupy the region above the relationship for SDSS SFGs with low SFRs < 0.1 M$_\odot$ yr^{-1} (Fig. 2a).

3.2 He II emission lines

Nebular helium emission line He II 4686 Å can be used as an indicator of hard ionizing radiation with the energy above 4 Ryd. The strong He II emission line often observed in galaxies with active star formation cannot always be explained by WR stars. These stars are detected only in a half of SFGs with the detected nebular He II emission (Guseva, Izotov & Thuan 2000; Thuan & Izotov 2005; Kehrig et al. 2015, 2018).

He II 4686 Å emission lines with intensities above 2 per cent of Hβ are observed in ~10 per cent of SFGs by Thuan & Izotov (2005).
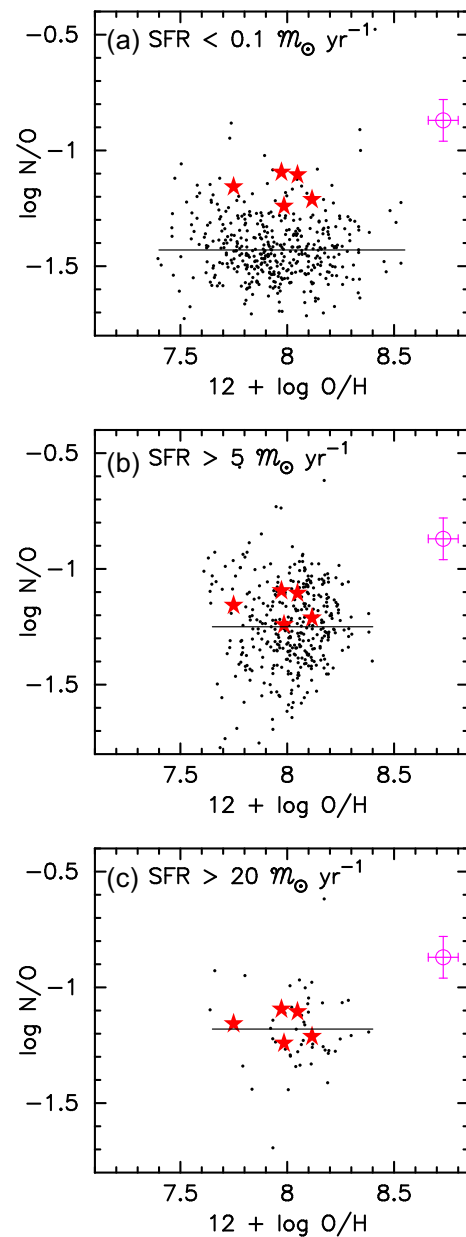

Figure 2. Dependence of the N/O abundance ratio on 12 + log O/H for three different ranges of SFR (derived from the extinction-corrected Hβ luminosities following Kennicutt 1998) for our LyC leakers and SFGs from the SDSS DR14. Symbols and samples are the same as in Fig. 1. Mean values of log N/O for the respective ranges of SFR are denoted by horizontal lines.

Such intense emission cannot be explained by photoionization models of H II regions ionized by stellar radiation powered by 'normal', known stellar populations. This problem of nebular He II emission is well known and has been widely discussed in the literature (e.g. Schaerer 1996; Guseva et al. 2000; Shirazi & Brinchmann 2012). Different possible explanations have been put forward, including 'uncommon' stellar populations, shocks, and X-ray binaries (see Kehrig et al. 2015, 2018; Szecsi et al. 2015; Götberg et al. 2018; Izotov et al. 2019; Plat et al. 2019; Schaerer, Fragos & Izotov 2019; Bian et al. 2020), although a consensus has not yet been reached.

Nebular He II emission, with intensity ratios ~0.8–2 per cent of Hβ, is observed in the XShooter spectra of our five targets. Although weaker than in some SFGs from the Thuan & Izotov (2005) sample,
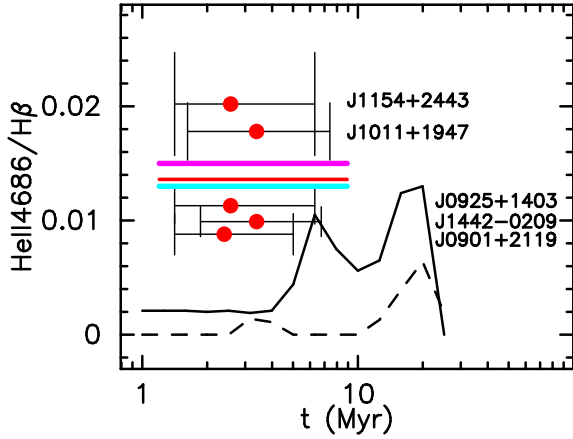
Figure 3. Dependence of the He II 4686/Hβ ratios on the starburst age. CLOUDY v17.01 models in conjunction with the BPASS v2.1 stellar population models from Izotov et al. (2019) for the instantaneous burst with the heavy element mass fraction of 10^{-5} (10^{-3}) and nebular oxygen abundance $12 + \log$ O/H = 7.0 are shown by the solid (dashed) line. The observed XShooter He II 4686/Hβ flux ratios are shown by red filled circles with error bars. Cyan and magenta lines indicate the position of local analogues of high-redshift galaxies and low-redshift reference galaxies, respectively, both selected from SDSS by Bian et al. (2020) (see details in the text) together with the mean He II/Hβ ratio for our leakers (red line).

these intensities are higher than predicted e.g. from BPASS models, even at very low metallicities. This is illustrated in Fig. 3, where we show stellar population models taken from Izotov et al. (2019) who considered BPASS v2.1 stellar models (Eldridge et al. 2017) with heavy element mass fraction of 10^{-3} and 10^{-5}, and nebular oxygen abundance $12 + \log$(O/H) = 7.0 together with the CLOUDY v17.01 model calculations for the instantaneous burst (Ferland et al. 2017) to obtain the dependence of the He II λ4686/Hβ emission line ratio with age. Stellar masses and ages of SFGs are derived from spectral energy distribution (SED) fitting of the SDSS spectra (see for more details, e.g. Izotov et al. 2016b). Indeed, the He II λ4686/Hβ emission line ratios in our LyC leakers are higher than those predicted by the models with heavy element mass fraction 10^{-3} and even with 10^{-5} (dashed and solid lines, respectively, in Fig. 3).

We compare He II λ4686/Hβ for our LyC leakers with that of the local analogues of high-z galaxies by Bian et al. (2020). The mean value of $\log$ [N II] λ6584/Hα for our LyC leakers range from –1.9 to –1.4. We selected from Bian et al. (2020) stacked values of He II 4686/Hβ for local analogues of high-z galaxies and for low-z reference SFGs only the data that are in the same range of [N II] λ6584/Hα. In Fig. 3 they are shown together with the mean He II λ4686/Hβ value for our leakers. All averaged values are nearly the same. Thus, the hard ionizing radiation in the high-z analogues and our LyC leakers are similar to that in local reference SFGs. However, there is so far no indication for a possible link between the hardness of the ionizing radiation and LyC leakage.

3.3 Mg II and Fe II* emission

Henry et al. (2018) have shown that the Lyα escape fraction in local compact SFGs tightly correlates with the Mg II $\lambda\lambda$2796, 2803 Å escape fraction. This implies that the Mg II $\lambda\lambda$2796, 2803 Å emission lines can be considered as a promising indicator of escaping Lyα and LyC emission. The Mg II emission lines are observed in all five our galaxies. Additionally, non-resonant Fe II* λ2612 and λ2626 emission lines are detected in three galaxies. We note that Fe II*

emission is observed in the galaxies with the strongest Mg II emission (Table A1). Indeed, the average dereddened flux of Mg II λ2796 emission in our three galaxies with detected Fe II* emission is ~20 per cent of the Hβ flux, while the average flux of Mg II λ2796 emission in the two galaxies without Fe II* emission is ~10 per cent of the Hβ. A similar behaviour is found in z = 1–2 galaxies by Erb et al. (2012). Mg II emission with P Cygni profiles and Fe II* emission can be tracers of galactic outflows (e.g. Finley et al. 2017). This emission may also originate in the H II region (Guseva et al. 2013, 2019; Finley et al. 2017; Henry et al. 2018). However, we do not detect P Cygni profiles in any emission lines including Mg II lines. Instead, we detect signs of high-velocity winds created by massive stars and/or supernova remnants (SNRs) in all our galaxies as indicated by broad emission components underlying the bright hydrogen lines and brightest forbidden lines of ions of some heavy elements. A more detailed study of these features will be discussed in a subsequent publication (Amorín et al., in preparation).

Mg II and Fe II* emission in our confirmed LyC leakers follows the same relations with global galaxy properties as other samples of SFGs with Mg II and Fe II* detections (Finley et al. 2017; Feltre et al. 2018; Guseva et al. 2019). Our galaxies with very young starbursts (EW(Hβ) = 180–350 Å) are located in the upper part of the SFR–$M_\star$ relation (Fig. 4a). These galaxies (excluding J0901+2119) are among the Mg II galaxies that deviate most from the main star formation sequence by Finley et al. (2017). For a given stellar mass, our galaxies tend to have high SFRs (by more than one order of magnitude higher than that for main-sequence galaxies).

The average stellar mass of three galaxies from the LyC leakers sample with the Fe II* detection is 2.67×10^9 M$_\odot$ or ~5 times higher than the average stellar mass of two galaxies without Fe II* emission (5.8×10^8 M$_\odot$, see Table 1), similarly to Finley et al. (2017), who found that Fe II* emission is preferentially seen in high-mass galaxies compared to galaxies with only Mg II emission. At the same time the average LyC escape fraction f_{esc}(LyC) from the Fe II* emitting high-mass galaxies (f_{esc}(LyC) = 5.9 per cent) is ~5 times lower than that for non-Fe II* emitting lower mass galaxies (f_{esc}(LyC) = 28.7 per cent). Here for averaging we have used the f_{esc}(LyC) values obtained by Izotov et al. (2016a,b, 2018a,b) from the *HST* COS spectra.

Guseva et al. (2019) considered the dependence of magnesium-to-neon abundance ratios on metallicity for a sample of more than 4000 Mg II emitting low-metallicity SFGs extracted from the SDSS DR14 and derived depletion of magnesium comparing this ratio with the solar abundance ratio of this moderately refractory element to noble neon. They obtained [Mg/Ne] = $\log$(Mg/Ne) – $\log$(Mg/Ne)$_\odot \simeq$ –0.4 at solar metallicity. We wish to check their conclusion adding the more precise XShooter data. In Fig. 4(b), we plot the SDSS DR14 Mg II sample but including only galaxies with abundances derived with the direct T_e method and with [O III] λ4363 fluxes measured with accuracy better than 4σ. The new data definitely follow the trend depicted by DR14 Mg II sample despite the smaller metallicity range of the LyC leakers. Thus, the LyC leakers have the same Mg II properties as a large Mg II sample with unknown LyC escape fractions.

Nakajima & Ouchi (2014) proposed to use O32 = [O III] λ5007/[O II] λ3727 as a parameter indicating the fraction of escaping ionizing radiation from density-bounded H II regions. Since that time many attempts have been made to find correlations between these two parameters. Both observational results (de Barros et al. 2016; Izotov et al. 2018b, 2020; Naidu et al. 2018) and model calculations (Bassett et al. 2019; Katz et al. 2020) increasingly indicate that O32 alone is an insufficient indicator of ionizing radiation
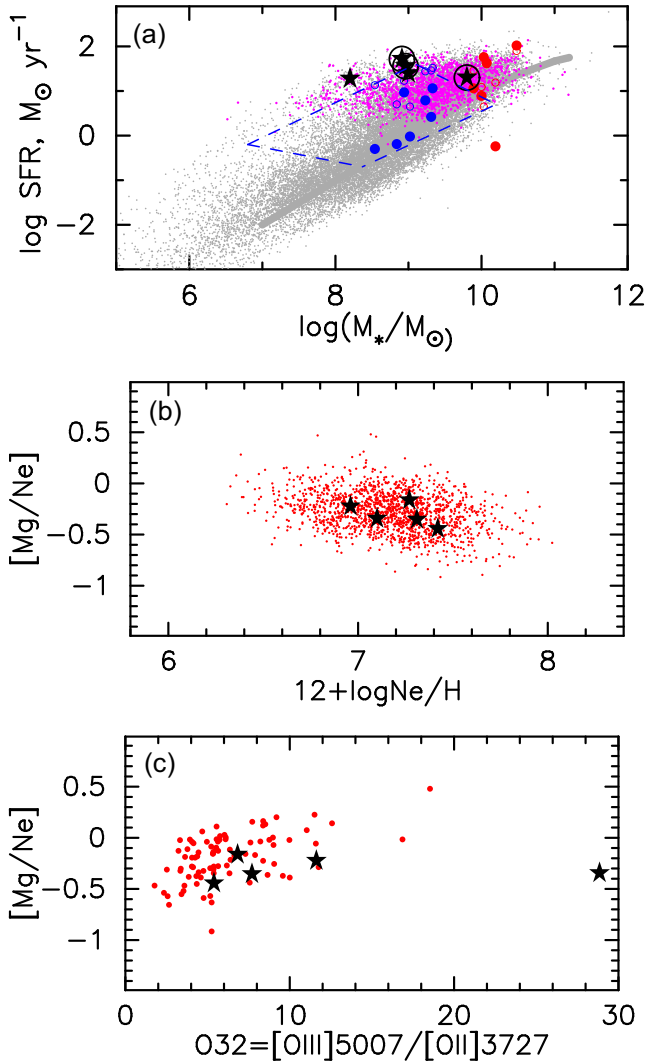
Figure 4. (a) Dependence of SFR on stellar mass $M_\star$. Five our sample galaxies with Mg II emission are shown by large black stars. Three galaxies with both Mg II and Fe II* emission in their spectra are encircled by black circles. The entire Mg II sample from Guseva et al. (2019) with high excitation H II regions with element abundances derived by the direct T_e method is shown by magenta dots. Additionally, SDSS DR14 SFGs with EW(Hβ) > 20 Å are shown by grey dots. The main sequence of SFGs of Finley et al. (2017) is indicated by thick grey line and their Mg II and Fe II* emitters are shown by blue and red circles, where filled and open circles indicate galaxies with SFRs derived by different methods. The location of Mg II emitters from Feltre et al. (2018) is indicated by dashed blue region. (b) Dependence of the magnesium-to-neon abundance ratio expressed in [Mg/Ne] $\equiv$ log Mg/Ne – log (Mg/Ne)$_\odot$ on the neon abundance 12 + log Ne/H. Only galaxies from SDSS DR14 Mg II sample with element abundances derived by the direct T_e method are shown (red dots). (c) Dependence of [Mg/Ne] on O32 = [O III] λ5007/[O II] λ3727. Symbols are the same as in (b) but for Mg II sample collected from DR14 only the galaxies with [O III] λ4363 intensity derived with accuracy better than 4σ, with abundances derived by the direct T_e method and with EW(Hβ) > 180 Å are shown (red dots).

leakage. Therefore, it is necessary to look for other additional indirect indicators of the LyC escape. Nevertheless, O32 is still potentially useful, albeit it is an insufficient f_{esc}(LyC) indicator. Therefore, it is of interest to study the behaviour of this indirect indicator in various dependences with other parameters.

A comparison of the empirical dependences between O32 and [Mg/Ne] made by Guseva et al. (2019) with the data for our galaxy sample is shown in Fig. 4(c). In the figure only galaxies with the parameters closest to those for our LyC leakers sample were selected from our DR14 sample, i.e. we used galaxies with EW(Hβ) > 180 Å. In this case the mean value is [Mg/Ne] = −0.19 for 86 DR14 Mg II emitting galaxies. If we restrict the selection from DR14 by the condition for the EW(Hβ) > 350 Å when dust grains likely would be destroyed by hard intense ultraviolet (UV) radiation, the mean value of [Mg/Ne] for remaining nine DR14 galaxies is near zero (–0.08) at its mean metallicity of 12 + logO/H = 7.8. As Izotov et al. (2011a, 2014b,c) showed, the presence of such large EW(Hβ) leads to effective warming-up and destruction of interstellar dust grains. For LyC leakers the average [Mg/Ne] is equal to –0.31 at its mean metallicity of 12 + logO/H = 8.0. Given the similarity of metallicities and EW(Hβ) in the two samples, the differences between mean [Mg/Ne] could be explained by low neutral hydrogen column density N(H I) in XShooter leakers or by possible different geometry of the neutral gas distribution. Note also that the mean SFR of our LyC leakers is two times higher than that of the nine galaxies from the DR14 sample.

Four of our galaxies with O32 < 12 tentatively follow the trend derived from the DR14 sample while one galaxy with O32 ∼ 30 is located considerably lower compared to that expected from the trend. However, it must be emphasized that our XShooter sample is small to give fairly definite conclusions.

3.4 BPT diagram and related diagnostics

Ongoing searches for the evolution of the properties of galaxies with redshift led to the discovery of so-called an 'offset' in the BPT diagram (Baldwin, Phillips & Terlevich 1981) between the locus of high-z galaxies and that of typical local galaxies. The interpretation of the BPT diagram (i.e. the O3N2 diagram) is also important in connection with applicability of the strong line methods developed for local galaxies to determine metallicity and other physical parameters for distant galaxies. Recent investigations of high-redshift galaxies based on large samples, specifically on the Keck Baryonic Structure Survey (KBSS; Steidel et al. 2014) and the MOSFIRE Deep Evolution Field (MOSDEF) survey (Kriek et al. 2015), have confirmed the offset of high-z galaxies compared to the typical local SFGs.

Several explanations for such offsets have been put forward, including a higher ionization parameter, harder ionizing spectra, higher electron number densities N_e (Steidel et al. 2014; Hayashi et al. 2015; Strom et al. 2017, 2018; Shapley et al. 2019), higher N/O abundance ratios at a given O/H in high-z galaxies (Andrews & Martini 2013; Masters et al. 2014; Kojima et al. 2017; Shapley et al. 2019; Loaiza-Agudelo et al. 2020), younger ages of the ionizing population (e.g. Hayashi et al. 2015; Topping et al. 2020), or combinations thereof. Photoionization models show that variations of one or several of these parameters can in principle explain the observed offsets (Kewley et al. 2013; Steidel et al. 2014; Sanders et al. 2016). Although the most recent studies seem to favour harder ionizing spectra or higher ionization parameters, no clear consensus on the dominant factor(s) has yet been reached (see e.g. Bian et al. 2020; Sanders et al. 2020).

We use the new XShooter observations of five confirmed LyC leakers with high f_{esc}(LyC) ∼ 3–46 per cent to construct the BPT diagram with more accurate line intensity measurements. For the remaining galaxies from the Izotov et al. (2016a,b, 2018a,b) sample (six galaxies, f_{esc}(LyC) ∼ 2–73 per cent) the SDSS data were used.
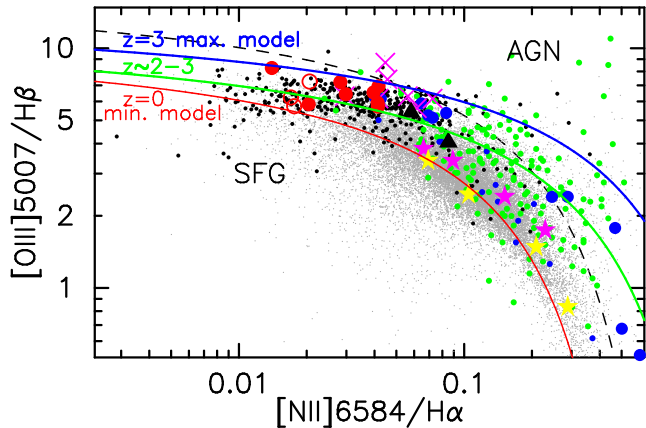
Figure 5. Baldwin–Phillips–Terlevich (BPT) diagnostic diagram (Baldwin et al. 1981) for 11 confirmed LyC leakers discovered by Izotov et al. (2016a,b, 2018a,b) including the new XShooter measurements. The leakers with an accuracy better than 5σ for the weak [N II] λ6584 Å emission lines are shown by red filled circles, the remaining ones by red open circles. Nearly 30 000 compact SFGs from SDSS DR14 are shown by grey dots from which the galaxies with large equivalent widths (EWs) of Hβ (EW(Hβ) > 180 Å) and accuracy of [N II] λ6584 flux measurements better than 5σ are presented by small black circles. Three Green Pea (GP) galaxies by Amorin et al. (2012a) observed with Gran Telescopio de Canarias (GTC)/Optical System for Imaging and low Resolution Integrated Spectroscopy (OSIRIS) are presented by large black triangles. Large blue circles are VLT/XShooter data for Lyman break analogues (LBAs) from Loaiza-Agudelo et al. (2020) selected as having large offset in the BPT diagram. LBAs of Overzier et al. (2009) are denoted by small blue circles. We also show $z = 2$–3 SFGs from KBSS/MOSFIRE sample by Steidel et al. (2014) (green circles) and MOSDEF stacked galaxies from Shapley et al. (2019) ($z \sim 2$–3, magenta stars, and $z \sim 1.5$, yellow stars). UV-selected SFGs with the extreme emission line ratios at $z \sim 2$ of Erb et al. (2016) are shown by magenta crosses. The separation line between SFGs and active galactic nuclei (AGN) by Kauffmann et al. (2003) is plotted as a dashed black curve. The minimum values (position of local galaxies at $z \sim 0$ along the star-forming branch) and maximum values (SFGs at $z = 3$) derived from theoretical models of Kewley et al. (2013) are represented by red and blue lines, respectively. The best fit to the entire KBSS sample of SFGs is drawn by the green curve (equation 9 from Steidel et al. 2014).

All LyC leakers with flux accuracy of the weakest emission line [N II] λ6584 Å exceeding 5σ are emphasized by red filled circles, the rest galaxies are shown by open circles in Fig. 5. The reference sample of $\sim$30 000 compact SFGs from SDSS DR14 is shown by grey dots. We note that the Hβ EW in all 11 LyC leakers is high, 180–430 Å. Therefore, for a better comparison of our sample with the reference sample, the SDSS SFGs with EW(Hβ) > 180 Å are denoted in the figure by black dots. In principle, the hardness of ionizing spectrum can be tested using the [O II]/[O III] versus [S III]/[S II] relation, as shown by Pérez-Montero, García-Benito & Vílchez (2019). However, these sulfur lines fall in the wavelength range of strong telluric absorption lines distorting XShooter observed fluxes.

For a comparison we also show local sample of Lyman break analogues (LBAs) by Overzier et al. (2009), LBAs observed with the VLT/XShooter by Loaiza-Agudelo et al. (2020), high-redshift ($z = 2$–3) SFGs from KBSS/MOSFIRE sample by Steidel et al. (2014), and MOSDEF stacked galaxies from Shapley et al. (2019).

As shown in Fig. 5, our local LyC leakers ($z \sim 0.3$–0.4) are located in the upper part of a SFG branch of the BPT diagram, coinciding with the position of LBAs from Overzier et al. (2009) and Loaiza-Agudelo
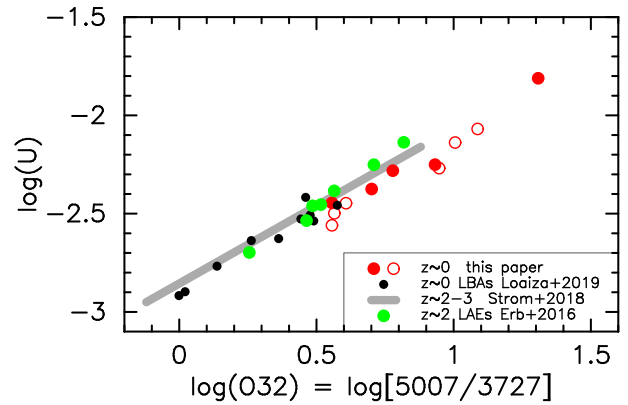

Figure 6. Relation between the ionization parameter $U = q/c$ estimated following Kobulnicky & Kewley (2004) and O32 for the confirmed LyC leakers discovered by Izotov et al. (2016a,b, 2018a,b) (red symbols, where filled circles denote objects for which metallicity is derived from XShooter data). Black circles are VLT/XShooter data for Lyman break analogues (LBAs) from Loaiza-Agudelo et al. (2020). Lyman α emitters (LAEs) from Erb et al. (2016) are denoted by green circles. The relation by Strom et al. (2018) derived for all KBSS/MOSFIRE SFGs at $z \sim 2$–3 is presented by a straight line.

et al. (2020) and that of high-z SFGs from Steidel et al. (2014) and Erb et al. (2016). The distribution of the LyC leakers overlaps with the upper part of the distribution of compact SDSS SFGs with EW(Hβ) > 180 Å (black dots). All these galaxies are located in the region corresponding to high-ionization parameters and hard UV ionizing radiation (Kewley et al. 2013; Steidel et al. 2014), and are offset with respect to the position of the typical local SFGs. Our LyC leakers have also high-ionization parameters in the range of log(U) = –2.5–1.7, relatively high N/O abundances, and high average ionizing photon production efficiencies $\xi = 10^{25.54}$ Hz erg^{-1} (see text below). Note that the high-z galaxies from Shapley et al. (2019) and the majority of high-redshift galaxies from Steidel et al. (2014) are located in the low-excitation part of the BPT diagram for SFGs. From the above discussion we conclude that the extreme galaxies both at low- and high-z are located in the same upper part of the BPT diagram for SFGs, which indicates similar physical conditions. From our data we cannot identify a single dominant mechanism that explains the observed offset in the BPT diagram.

3.4.1 Ionization parameter

The ionization state of the gas in galaxies is characterized by the ionization parameter q or by the dimensionless ionization parameter $U = q/c$ that is the ratio of the number density of ionizing photons to the number density of hydrogen. The O32 ratio (here O32 is defined as [O III] λ5007/[O II] λ3727) can serve as an observational indicator of the ionization parameter. Since the oxygen abundances O/H of our LyC leakers were determined with high accuracy of 0.02–0.03 dex (see Table 3), we calculated U following Kobulnicky & Kewley (2004) (their equation 13), and using new strong line measurements and metallicities. In Fig. 6, the relation between U and O32 for these galaxies is shown by red filled circles, where the remaining LyC leakers from Izotov et al. (2016a,b, 2018a,b) are denoted by open red circles. They have a similar slope but consist of some galaxies with higher U and O32 compared to the sequence outlined by local LBAs from Loaiza-Agudelo et al. (2020) (black circles) and $z \sim 2$ LAEs by Erb et al. (2016) (green circles). Higher U for some of our
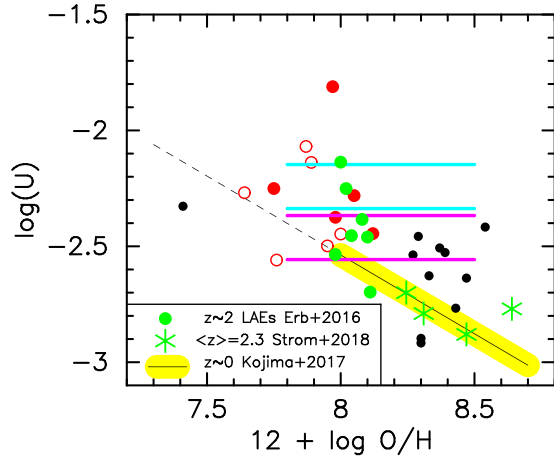
Figure 7. Dependence of the ionization parameter U on $12 + \log O/H$ for the same data as in Fig. 6. Additionally, median values of U in equal number bins of $12 + \log O/H$ for $148 <z> = 2.3$ KBSS galaxies from Strom et al. (2018) are shown by green asterisks. The relation by Kojima et al. (2017) (their equation 13) derived as the best fit to the local $\sim200\,000$ SFGs stacked in $M_\star$ and SFR by Andrews & Martini (2013) is shown by yellow and solid black lines. The extrapolation of the best-fitting linear function of Kojima et al. (2017) to lower metallicities is denoted by a dashed line. Cyan and magenta lines show the position of local analogues of high-z galaxies and low-redshift SDSS reference galaxies, respectively, by Bian et al. (2020).

LyC leakers is probably the result of our selection of candidates to the leakers based on high O32. Our sample has a lower metallicity, with an average value of $12 + \log O/H = 7.9$ for 11 LyC leakers compared to 8.3 for the LBAs and slightly lower compared to 8.05 for the LAEs (Fig. 7).

We have also compared the behaviour of the ionization parameter as a function of metallicity between our local LyC leakers, $z \sim 2$ LAEs (Erb et al. 2016), local LBAs (Loaiza-Agudelo et al. 2020), and $\sim200\,000$ local SFGs from SDSS DR7 of Kojima et al. (2017) (Fig. 7). We also show dependence of the ionization parameter on nebular metallicity for 148 high-z KBSS galaxies by Strom et al. (2018) ($<z> = 2.3$) represented by median values in equal number bins of the oxygen abundance (green asterisks). Our data clearly show lower metallicities and higher ionization parameters compared to high-z and other local samples of typical SFGs and slightly lower metallicities and higher ionization parameters for some LyC leakers compared to $z \sim 2$ LAEs by Erb et al. (2016).

3.4.2 Ionizing photon production efficiency ξ

The ionizing photon production efficiency of galaxies ξ is defined as the ratio of the number of ionizing photons produced per unit time $N(\text{LyC})$ (production rate) to the intrinsic monochromatic UV luminosity L_ν per unit frequency, commonly measured at rest-frame wavelength $\lambda = 1500$ Å. The production rate is calculated as $N(\text{LyC}) = 2.1 \times 10^{12} L(\text{H}\beta)$, following Storey & Hummer (1995). The uncertainty of the ξ determinations in all our galaxies is less than 10 per cent.

ξ is important to constrain the properties of galaxies during the reionization of the Universe. The efficiency of ionizing photon production quantifies also the relative amount of massive ionizing stars with respect to the number of less massive non-ionizing stars present in a galaxy. Together ξ, the LyC escape fraction, and the UV luminosity density allow one to calculate if the sources considered
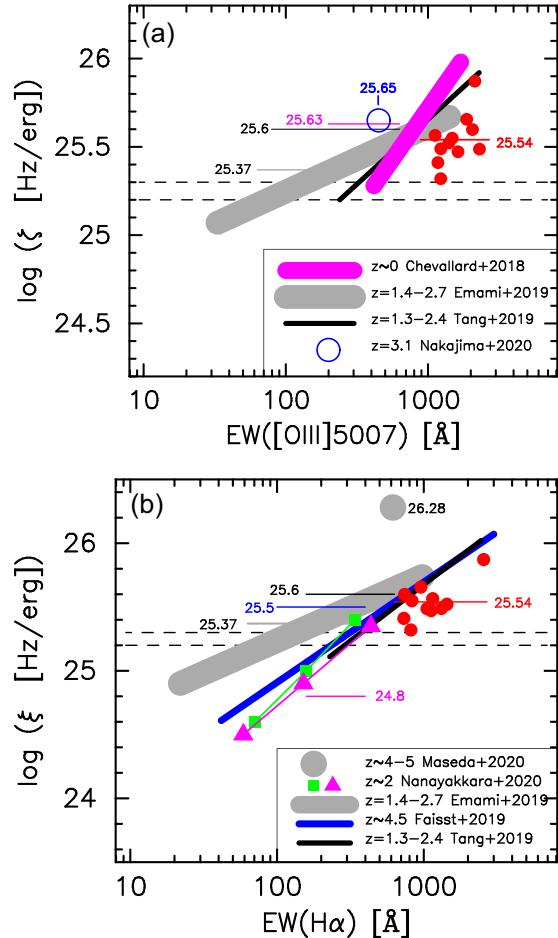

Figure 8. Relation between the ionizing photon production efficiency ξ and EW([O III] $\lambda5007$) (a) and EW(Hα) (b). Our LyC leakers are shown by red circles. The thick grey line in (a) is the best fit to the sample of low-mass ($\sim 10^{9.5}$ M$_\odot$) galaxies at $z = 1.4$–2.7 from Emami et al. (2020). The position of extreme [O III] emitters from Tang et al. (2019) is denoted by the black line. The LyC–LAE subsample (stacked LAEs with a clear LyC detection) of the LymAn Continuum Escape Survey (LACES) at $z \sim 3.1$ from Nakajima et al. (2020) is shown by the large open blue circle. The sample of local analogues of high-z galaxies by Chevallard et al. (2018) is represented by the thick magenta line. (b) Data for high-z galaxies of Emami et al. (2020), Faisst et al. (2019), and Tang et al. (2019) are shown by thick grey, blue, and black lines, respectively. Galaxies at $z \sim 2$ from Nanayakkara et al. (2020) are shown by green squares (entire sample) and magenta triangles (Hβ detected galaxies). Using stacked *Spitzer*/Infrared Array Camera (IRAC) photometry for $z \sim 4$–5 galaxies, Maseda et al. (2020) determined $\log(\xi/[\text{erg}^{-1}\,\text{Hz}]) = 26.28$ (large grey filled circle). The canonical values of $\log(\xi/[\text{erg}^{-1}\,\text{Hz}]) = 25.2$–25.3 from Robertson et al. (2013) and Bouwens et al. (2016), respectively, are shown by black dashed horizontal lines in (a) and (b). Average values of $\log \xi$ for different samples are denoted by corresponding positions of coloured horizontal lines and are labelled with the corresponding quantities.

(galaxies) are sufficient to reionize the Universe (see e.g. Naidu et al. 2020).

In Fig. 8, we show the dependence of the ionizing photon production efficiency ξ on EW([O III] $\lambda5007$) and on EW(Hα) for our sample of 11 confirmed LyC leakers (Izotov et al. 2016a,b, 2018a,b). It is interesting to compare our data with those for other local and high-z samples. For example, 130 Hα detections from ZFIRE survey using KECK/MOSFIRE give a median $\log(\xi/[\text{erg}^{-1}\,\text{Hz}]) = 24.8$ for galaxies at $z \sim 2$ within the mass range of 10^9–3×10^{11} M$_\odot$ (Nanayakkara

et al. [2020]). Emami et al. ([2020]) derived $\log(\xi/[\mathrm{erg}^{-1}\,\mathrm{Hz}]) = 25.37$ for a mass-complete sample $(7.8 < \log(M_\star/M_\odot) < 9.8)$ in the redshift range 1.4–2.7. The sample of 221 $z \sim 4.5$ galaxies at $\log M_\star/M_\odot > 9.7$ (Faisst et al. [2019]) spans a large range of ξ with a median $\log(\xi/[\mathrm{erg}^{-1}\,\mathrm{Hz}]) \sim 25.5$. This is ~ 0.3 dex higher than the typically assumed canonical value $\log(\xi/[\mathrm{erg}^{-1}\,\mathrm{Hz}]) = 25.3$ (Bouwens et al. [2016]). Extreme [O III] emitters by Tang et al. ([2019]) at $z = 1.3$–2.4 reach the largest values of $\log(\xi/[\mathrm{erg}^{-1}\,\mathrm{Hz}]) \sim 25.6$ for the galaxies with highest EW(Hα) > 1000 Å. The sample of 10 extreme nearby SFGs by Chevallard et al. ([2018]) shows a similar slope and range of ξ and EWs of strong emission nebular lines as high-z SFGs.

The galaxies in our sample cover too small a range in EW(Hα) and EW([O III] λ5007) to determine the slope of the relation, but together with the galaxies from Chevallard et al. ([2018]) they follow a relatively steep relation, close to the relation for high-z galaxies. All our LyC leakers have ξs that are among the highest compared to the high-z samples (Faisst et al. [2019]; Tang et al. [2019]; Emami et al. [2020]; Nanayakkara et al. [2020]) and local ones (Chevallard et al. [2018]). This echoes Chevallard et al. ([2018])'s conclusions that there is not strong evolution of the relation between ξ and EW(Hβ) or EW([O III] λ5007) over $0 \lesssim z \lesssim 2$. The strong increase of the ionizing photon production with increasing EW of strong nebular emission lines means that extreme galaxies such as compact SFGs with maximal EWs or their subset of LyC leakers might be important contributors to reionization of the early Universe.

3.5 He I emission line diagnostic

Recently Izotov et al. ([2017]) proposed a new approach to estimate the neutral hydrogen column density N(H I) based on flux ratios of He I emission lines $I(\lambda 3889)/I(\lambda 6678)$ and $I(\lambda 7065)/I(\lambda 6678)$, which helps to qualitatively conclude whether the galaxy can be a Lyα and LyC leaker. Low average H I column densities, low column-density channels in dense environment, or a diversity of geometries and neutral gas porosity (low H I covering fractions), or a combination thereof (Kakiichi & Gronke [2019]; Kimm et al. [2019]; Gazagnes et al. [2020]) can be important for the escape of ionizing photons. The proposed method has been tested on several galaxies (Izotov et al. [2020]). The disadvantage of this method – that it relies on emission lines of relatively low intensities – can be circumvented by observing them with large telescopes and sufficient S/N ratio, as the case for our VLT/XShooter observations, where the S/N ratio for the helium lines is ~ 20–30.

In Fig. [9], we show the relation between the He I emission line ratios for our confirmed LyC leakers (XShooter data, red circles) and for the Large Binocular Telescope (LBT) sample of lower redshift ($z < 0.1$) LyC leaker candidates of Izotov et al. ([2017]) (black circles). Additionally, we present confirmed LyC leakers of Izotov et al. ([2016b], [2018b]) for which He I fluxes were measured from the SDSS spectra (grey circles). For the leaker candidates from Izotov et al. ([2017]), $f_{\rm esc}$(LyC) was estimated using velocity separation $V_{\rm sep}$ between the two peaks of Lyα emission line profiles (Izotov et al. [2020]); galaxies where the Lyα line profile consists of the emission line superimposed on broad absorption were excluded.

From Fig. [9] we see that almost all the galaxies shown are located in the region of low N(H I), according to the CLOUDY models (solid and dashed lines). The lines shown are CLOUDY models for a burst of star formation with age $t = 2$ Myr, fixed ionization parameter,
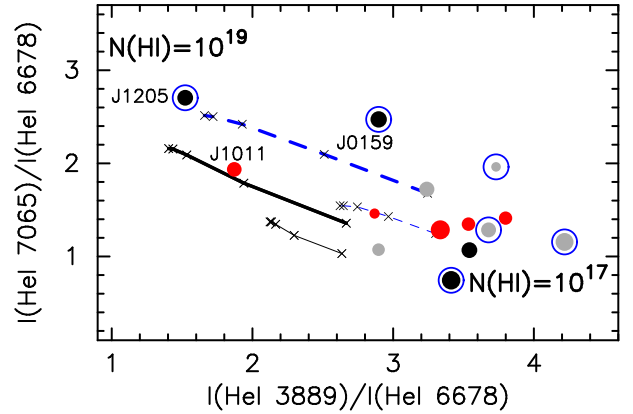

Figure 9. Diagnostic diagram for He I λ3889/λ6678 versus λ7065/λ6678 intensity ratios proposed by Izotov, Thuan & Guseva ([2017]) for our sample shown by red circles. Confirmed LyC leakers from Izotov et al. ([2016b], [2018b]) and Lyα emitting galaxies from Izotov et al. ([2020]) with He I fluxes measured from the SDSS spectra are shown by grey dots (the exception is J1333+6246 with a very noisy spectrum, which was discarded from the analysis). The Large Binocular Telescope (LBT) spectrophotometric observations of the lowest z candidates to leakers with extremely high O32 in the range of 23–43 (Izotov et al. [2017]) are denoted by black symbols. Galaxies with oxygen abundances $12 + \log O/H < 7.75$ are encircled with blue circles. All symbol sizes scale with $f_{\rm esc}$(LyC) derived either through direct LyC observations (Izotov et al. [2016a,b], [2018a,b]) or using velocity separation between peaks, $V_{\rm sep}$, in Lyα emission profiles (Izotov et al. [2020]). CLOUDY models for a burst of star formation with age $t = 2$ Myr, fixed ionization parameter, filling factor $\log f = -0.5$, oxygen abundance $12 + \log O/H = 7.3$ (blue dashed) and 8.0 (black solid), and with two values of the electron number density $N_{\rm e} = 1000$ (thick) and 100 cm^{-3} (thin) are shown by lines. Crosses on the lines mark increase of neutral hydrogen column densities from N(H I) $= 10^{17}$ to 10^{19} cm^{-2} in 0.5 dex (from right to the left).

filling factor $\log f = -0.5$, oxygen abundances $12 + \log O/H = 7.3$ (blue dashed line) and 8.0 (black solid line), and with two values of the electron number density, $N_{\rm e} = 1000$ (thick lines) and 100 cm^{-3} (thin lines). All model He I ratios in Fig. [9] are calculated for static H II regions. In the models with velocity gradients 3889/6678 and 7065/6678 ratios would be, respectively, higher and lower for a fixed N(H I), because of line Doppler broadening leading to lower optical depth of the 3889 transition.

The galaxy J1205+4551 is an exception. We note that this galaxy does not have a directly derived $f_{\rm esc}$(LyC), but only its estimation by using the value of $V_{\rm sep}$ (equation 2 in Izotov et al. [2018b]). Moreover, this galaxy is one of the most deviating objects in the relation between $f_{\rm esc}$(Lyα) and directly derived $f_{\rm esc}$(LyC) (see fig. 8 in Izotov et al. [2020]), and it is located on the relation $f_{\rm esc}$(Lyα) $= f_{\rm esc}$(LyC). Its oxygen abundance $12 + \log O/H = 7.46$ is one of the lowest among all galaxies shown in Fig. [9]. Two other galaxies marked in the figure, namely, J1011+1947 and J0159+0751, imply N(H I) $\geq 5 \times 10^{17}$ cm^{-2}. For the latter galaxy Izotov et al. ([2017]) have derived the highest electron density $N_{\rm e}$(He I) $= 2246$ cm^{-3} among the five compact SFGs with extremely high O32 observed with the LBT (Izotov et al. [2017]). J1011+1947 has the highest electron number density among our LyC leakers, both from sulfur and from oxygen determinations (Table [3]). Such high electron densities should move the galaxies upward following to the CLOUDY models.

Therefore, according to the diagram in Fig. [9], all our XShooter leakers and other confirmed LyC leakers (Izotov et al. [2016a,b], [2018a,b]) and the lowest z candidates (Izotov et al. [2017]) excluding

J1205+4551 indicate low H I column densities implying leakage of LyC radiation from these galaxies, likely due to their density-bounded H II regions. For comparison, Izotov et al. (2017) in their fig. 8 have shown the relation between the $I(\lambda3889)/I(\lambda6678)$ and $I(\lambda7065)/I(\lambda6678)$ ratios for non-LyCs (unpublished LBT data and data by Yang et al. 2017). All Lyα emitting galaxies from Yang et al. (2017) and the vast majority of blue compact dwarf galaxies (BCDs) with O32 $\sim$ 5–20, observed with the LBT, are located in the region of high $I(\lambda3889)/I(\lambda6678)$ and low $I(\lambda7065)/I(\lambda6678)$ ratios corresponding to the case of low column-density regions. However, there may be exceptions when ionization-bounded galaxies with very high ionization parameter have also high average N(H I), as it likely is in the case of J1205+4551, but low-density channels are present through which the ionizing radiation can escape (Kakiichi & Gronke 2019; Kimm et al. 2019). This suggests that the diagnostic method proposed by Izotov et al. (2017) can effectively indicate LyC leakage.

4 SUMMARY

We have obtained new VLT/XShooter spectra of five confirmed LyC leakers at $z \sim 0.3$–4 discovered recently with the *HST*. Using the spectra we study the physical properties of these compact SFGs, which have many similar parameters with extreme high-z galaxies responsible for reionization of the early Universe. Our main findings are the following.

(1) Our XShooter LyC leakers have the same distributions of Ne/O, S/O, Ar/O, Fe/O, and Mg/O abundance ratios with oxygen abundance as other samples of SFGs. An exception is the N/O abundance ratio, which is enhanced compared to the bulk of nearby SFGs in the oxygen abundance range $12 + \log \text{O/H} \simeq 7.7$–8.1 with the mean value of $\log \text{N/O} = -1.16$. This value is similar to that found in other local and high-z analogues of galaxies of the epoch of reionization.

(2) We find mean electron densities $N_e \sim 400 \text{ cm}^{-3}$, which are significantly higher (by a factor of 10 or more) than those typical for local SDSS SFGs, and are comparable to those measured in SFGs at $z \sim 2$–3.

(3) We detect the nebular He II $\lambda4686$ Å emission line in all our galaxies with intensities of 1–2 per cent of the Hβ emission line, indicating a relatively hard ionizing spectrum in these galaxies, comparable to other galaxies at the same metallicity.

(4) Strong resonant Mg II $\lambda\lambda2796$, 2803 Å emission lines with $I(\lambda2796,2803)/I(\text{H}\beta) \simeq 10$–38 per cent and without P Cygni features are observed in all five our galaxies. Additionally non-resonant Fe II* $\lambda2612$ and $\lambda2626$ lines are detected in three of the five galaxies with stronger Mg II emission, higher $M_\star$ and with f_{esc}(LyC) $\sim$ 5 times lower than that for non-emitting Fe II* galaxies. Our LyC leakers show the same trend of [Mg/Ne] with metallicity as an entire DR14 Mg II sample exhibiting the same magnesium depletion in dust.

(5) The location of the 11 compact $z \sim 0.3$–0.4 LyC leakers (from which our sample is drawn) with EW(Hβ) = 180–430 Å in the BPT diagram coincides with the upper boundary of compact SDSS SFGs with EW(Hβ) > 180 Å, positions of local LBAs (Overzier et al. 2009; Loaiza-Agudelo et al. 2020), and $z \sim 2$–3 SFGs (Steidel et al. 2014; Erb et al. 2016). Our LyC leakers have high-ionization parameters $\log(U) = -2.5$ to -1.7 and high average ionizing photon production efficiencies $\xi = 10^{25.54}$ erg^{-1} Hz. Therefore, we conclude that the extreme galaxies at both low- and high-z reside in the same part of

the BPT diagram and have properties very similar to most extreme $z \sim 2$–3 galaxies.

(6) Using new measurements of faint He I lines, we confirm the effectiveness of the He I emission line diagnostic proposed by Izotov et al. (2017) to identify LyC leaking galaxies. All the LyC leakers from Izotov et al. (2016a,b, 2018a,b) and the low-z LyC leaker candidates of Izotov et al. (2017) except one (J1205+4551) are located in the region of low neutral hydrogen column density N(H I), which indicates leakage of LyC radiation from these galaxies.

DATA AVAILABILITY

The data underlying this paper are available in the paper and in its online supplementary material.

REFERENCES

Amorin R. O., Pérez-Montero E., Vílchez J. M., 2010, ApJ, 715, L128
Amorin R. O., Vílchez J. M., Pérez-Montero E., Papaderos P., 2012a, ApJ, 749, 185
Amorin R. O., Vílchez J. M., Pérez-Montero E., 2012b, in Papaderos P., Hensler G., Recchi S., eds, Astrophys. Space Sci. Proc. Vol. 28, Dwarf Galaxies: Keys to Galaxy Formation and Evolution. Springer-Verlag, Berlin, p. 243
Andrews B. H., Martini P., 2013, ApJ, 765, 140
Baldwin J. A., Phillips M. M., Terlevich R., 1981, PASP, 93, 5
Bassett R. et al., 2019, MNRAS, 483, 5223
Bayliss M. B., Rigby J. R., Sharon K., Wuyts E., Florian M., Gladders M. D., Johnson T., Oguri M., 2014, ApJ, 790, 144
Becker G. D., Bolton J. S., Lidz A., 2015, Publ. Astron. Soc. Aust., 32, 45
Bian F., Fan X., 2020, MNRAS, 493, L65
Bian F., Kewley L. J., Groves B., Dopita M. A., 2020, MNRAS, 493, 580
Bouwens R. J., Illingworth G. D., Blakeslee J. P., Broadhurst T. J., Franx M., 2004, ApJ, 611, L1
Bouwens R. J. et al., 2016, ApJ, 833, 72
Bowler R. A. A., Dunlop J. S., McLure R. J., McLeod D. J., 2017, MNRAS, 466, 3612

Cardelli J. A., Clayton G. C., Mathis J. S., 1989, ApJ, 345, 245

Castellano M. et al., 2017, ApJ, 839, 73

Charlot S., Longhetti M., 2001, MNRAS, 323, 887

Chevallard J. et al., 2018, MNRAS, 479, 3264

Christensen L. et al., 2012, MNRAS, 427, 1973

Curtis-Lake E. et al., 2016, MNRAS, 457, 440

de Barros S., Schaerer D., Stark D. P., 2014, A&A, 563, A81

de Barros S. et al., 2016, A&A, 585, A51

Dors O. L., Agarwal B., Hägele G. F., Cardaci M. V., Rydberg C.-E., Riffel R. A., Oliveira A. S., Krabbe A. C., 2018, MNRAS, 479, 2294

Duncan K. et al., 2014, MNRAS, 444, 2960

Eldridge J. J., Stanway E. R., Xiao L., McClelland L. A. S., Taylor G., Ng M., Greis S. M. L., Bray J. C., 2017, Publ. Astron. Soc. Aust., 34, 58

Emami N., Siana B., Alavi A., Gburek T., Freeman W. R., Richard J., Weisz D. R., Stark D. P., 2020, ApJ, 895, 116

Endsley R., Stark D. P., Chevallard J., Charlot S., 2020, preprint (arXiv: 2005.02402)

Erb D. K., Quider A. M., Henry A. L., Martin C. L., 2012, ApJ, 759, 26

Erb D. K., Pettini M., Steidel C. C., Strom A. L., Rudie G. C., Trainor R. F., Shapley A. E., Reddy N. A., 2016, ApJ, 830, 52

Faisst A. L., Capak P. L., Emami N., Tacchella S., Larson K. L., 2019, ApJ, 884, 133

Feltre A. et al., 2018, A&A, 617, A62

Ferguson H. C. et al., 2004, ApJ, 600, L107

Ferland G. J. et al., 2017, Rev. Mex. Astron. Astrofis., 53, 385

Finley H. et al., 2017, A&A, 608, A7

Fischer C. F., Tachiev G., 2014, MCHF/MCDHF Collection, Version 2, Ref. No. 10 and 20. National Institute of Standards and Technology. Available online at http://physics.nist.gov/mchf

Fletcher T. J., Tang M., Robertson B. E., Nakajima K., Ellis R. S., Stark D. P., Inoue A., 2019, ApJ, 878, 87

Gazagnes S., Chisholm J., Schaerer D., Verhamme A., Izotov Y., 2020, A&A, 639, A85

González V., Bouwens R., Illingworth G., Labbé I., Oesch p., Franx M., Magee D., 2014, ApJ, 781, 34

González-Delgado R. M., Leitherer C., Heckman T. M., 1999, ApJS, 125, 489

Götberg Y., de Mink S. E., Groh J. H., Kupfer T., Crowther P. A., Zapartas E., Renzo M., 2018, A&A, 615, A78

Grazian A. et al., 2015, A&A, 575, A96

Guseva N. G., Izotov Y. I., Thuan T. X., 2000, ApJ, 531, 776

Guseva N. G., Izotov Y. I., Stasińska G., Fricke K. J., Henkel C., Papaderos P., 2011, A&A, 529, A149

Guseva N. G., Izotov Y. I., Fricke K. J., Henkel C., 2012, A&A, 541, A115

Guseva N. G., Izotov Y. I., Fricke K. J., Henkel C., 2013, A&A, 555, A90

Guseva N. G., Izotov Y. I., Fricke K. J., Henkel C., 2015, A&A, 579, A11

Guseva N. G., Izotov Y. I., Fricke K. J., Henkel C., 2019, A&A, 624, A21

Harshan A. et al., 2020, ApJ, 892, 77

Hayashi M. et al., 2015, PASJ, 67, 80

Henry A., Berg D. A., Scarlata C., Verhamme A., Erb D., 2018, ApJ, 855, 96

Huang K.-H. et al., 2016, ApJ, 817, 11

Izotov Y. I., Thuan T. X., 2004, ApJ, 602, 200

Izotov Y. I., Thuan T. X., Lipovetsky V. A., 1994, ApJ, 435, 647

Izotov Y. I., Stasińska G., Guseva N. G., Thuan T. X., 2004, A&A, 415, 87

Izotov Y. I., Stasińska G., Meynet G., Guseva N. G., Thuan T. X., 2006, A&A, 448, 955

Izotov Y. I., Guseva N. G., Fricke K. J., Henkel C., 2011a, A&A, 536, L7

Izotov Y. I., Guseva N. G., Thuan T. X., 2011b, ApJ, 728, 161

Izotov Y. I., Thuan T. X., Guseva N. G., 2012, A&A, 546, A122

Izotov Y. I., Thuan T. X., Guseva N. G., 2014a, MNRAS, 445, 778

Izotov Y. I., Guseva N. G., Fricke K. J., Henkel C., 2014b, A&A, 561, A33

Izotov Y. I., Guseva N. G., Fricke K. J., Henkel C., 2014c, A&A, 570, A97

Izotov Y. I., Orlitová I., Schaerer D., Thuan T. X., Verhamme A., Guseva N. G., Worseck G., 2016a, Nature, 529, 178

Izotov Y. I., Schaerer D., Thuan T. X., Worseck G., Guseva N. G., Orlitová I., Verhamme A., 2016b, MNRAS, 461, 3683

Izotov Y. I., Thuan T. X., Guseva N. G., 2017, MNRAS, 471, 548

Izotov Y. I., Thuan T. X., Guseva N. G., Liss S. E., 2018a, MNRAS, 473, 1956

Izotov Y. I., Schaerer D., Worseck G., Guseva N. G., Thuan T. X., Verhamme A., Orlitová I., Fricke K. J., 2018b, MNRAS, 474, 4514

Izotov Y. I., Thuan T. X., Guseva N. G., 2019, MNRAS, 483, 549

Izotov Y. I., Schaerer D., Worseck G., Verhamme A., Guseva N. G., Thuan T. X., Orlitová I., Fricke K. J., 2020, MNRAS, 491, 468

James B. L. et al., 2014, MNRAS, 440, 1794

Jaskot A. E., Oey M. S., 2013, ApJ, 766, 91

Kakiichi K., Gronke M., 2019, preprint (arXiv:1905.02480)

Katz H. et al., 2020, preprint (arXiv:2005.01734)

Kauffmann G. et al., 2003, MNRAS, 341, 33

Kehrig C., Vílchez J. M., Pérez-Montero E., Iglesias-Páramo J., Brinchmann J., Kunth D., Durret F., Bayo F. M., 2015, ApJ, 801, L28

Kehrig C., Vílchez J. M., Guerrero M. A., Iglesias-Páramo J., Hunt L. K., Duarte-Puertas S., Ramos-Larios G., 2018, MNRAS, 480, 1081

Kennicutt R. C., Jr, 1998, ARA&A, 36, 189

Kewley L. J., Dopita M. A., Leitherer C., Davé R., Yuan T., Allen M., Groves B., Sutherland R., 2013, ApJ, 774, 100

Kimm T., Blaizot J., Garel T., Michel-Dansac L., Katz H., Rosdahl J., Verhamme A., Haehnelt M., 2019, MNRAS, 486, 2215

Kobulnicky H. A., Kewley L. J., 2004, ApJ, 617, 240

Kojima T., Ouchi M., Nakajima K., Shibuya T., Harikane Y., Ono Y., 2017, PASJ, 69, 44

Köppen J., Hensler G., 2005, A&A, 434, 531

Kriek M. et al., 2015, ApJS, 218, 15

Loaiza-Agudelo M., Overzier R. A., Heckman T., 2020, ApJ, 891, 19

Lodders K., 2020, preprint (arXiv:1912.00844)

Ma X., Quataert E., Wetzel A., Hopkins P. F., Faucher-Giguére C.-A., Kereš D., 2020, preprint (arXiv:2003.05945)

Maiolino R. et al., 2015, MNRAS, 452, 54

Maseda M. V. et al., 2020, MNRAS, 493, 5120

Masters D. et al., 2014, ApJ, 785, 153

Mollá M., Vílchez J. M., Gavilán M., Dáz A. I., 2006, MNRAS, 372, 1069

Naidu R. P., Forrest B., Oesch P. A., Tran K.-V. H., Holden B. P., 2018, MNRAS, 478, 791

Naidu R. P., Tacchella S., Mason C. A., Bose S., Oesch P. A., Conroy C., 2020, ApJ, 892, 109

Nakajima K., Ouchi M., 2014, MNRAS, 442, 900

Nakajima K., Ouchi M., Shimasaku K., Hashimoto T., Ono Y., Lee J. C., 2013, ApJ, 769, 3

Nakajima K., Ellis R. S., Robertson B. E., Tang M., Stark D. P., 2020, ApJ, 889, 161

Nanayakkara T. et al., 2020, ApJ, 889, 180

Oesch P. A. et al., 2010, ApJ, 709, L21

Ono Y. et al., 2012, ApJ, 744, 83

Ota K. et al., 2014, ApJ, 792, 34

Ouchi M. et al., 2013, ApJ, 778, 102

Overzier R. A. et al., 2009, ApJ, 706, 203

Paulino-Afonso A., Sobral D., Ribeiro B., 2018, MNRAS, 476, 5479

Pérez-Montero E., García-Benito R., Vílchez J. M., 2019, MNRAS, 483, 3322

Pilyugin L. S., Grebel E. K., Mattsson L., 2012, MNRAS, 424, 2316

Plat A., Charlot S., Bruzual G., Feltre A., Vidal-García A., Morisset C., Chevallard J., Todt H., 2019, MNRAS, 490, 978

Roberts-Borsani G. W. et al., 2016, ApJ, 823, 143

Robertson B. E. et al., 2013, ApJ, 768, 71

Salmon B. et al., 2015, ApJ, 799, 183

Sánchez-Almeida J., Pérez-Montero E., Morales-Luis A. B., Muñoz-Tuñón C., García-Benito R., Nuza S. E., Kitaura F. S., 2016, ApJ, 819, 110

Sanders R. L. et al., 2016, ApJ, 816, 23

Sanders R. L. et al., 2020, MNRAS, 491, 1427

Santini P. et al., 2017, ApJ, 847, 76

Schaerer D., 1996, ApJ, 467, L17

Schaerer D., de Barros S., 2009, A&A, 502, 423

Schaerer D., Boone F., Zamojski M., Staguhn J., Dessauges-Zavadsky M., Finkelstein S., Combes F., 2015, A&A, 574, A19

Schaerer D., Izotov Y. I., Verhamme A., Orlitová I., Thuan T. X., Worseck G., Guseva N. G., 2016, A&A, 591, L8

Schaerer D., Fragos T., Izotov Y. I., 2019, A&A, 622, L10

Shapley A. E. et al., 2019, ApJ, 881, L35

Shibuya T., Ouchi M., Harikane Y., 2015, ApJS, 219, 15

Shirazi M., Brinchmann J., 2012, MNRAS, 421, 1043

Smit R. et al., 2014, ApJ, 784, 58

Smit R. et al., 2015, ApJ, 801, 122

Stark D. P., 2016, ARA&A, 54, 761

Stark D. P., Schenker M. A., Ellis R., Robertson B., McLure R., Dunlop J., 2013a, ApJ, 763, 129

Stark D. P. et al., 2013b, MNRAS, 436, 1040

Stark D. P. et al., 2017, MNRAS, 464, 469

Steidel C. C. et al., 2014, ApJ, 795, 165

Steidel C. C., Strom A. L., Pettini M., Rudie G. C., Reddy N. A., Trainor R. F., 2016, ApJ, 826, 159

Storey P. J., Hummer D. G., 1995, MNRAS, 272, 41

Strom A. L., Steidel C. S., Rudie G. C., Trainor R. F., Pettini M., Reddy N. A., 2017, ApJ, 836, 164

Strom A. L., Steidel C. S., Rudie G. C., Trainor R. F., Pettini M., 2018, ApJ, 868, 117

Szecsi D., Langer N., Yoon S.-C., Sanyal D., de Mink S., Evans C. J., Dermine T., 2015, A&A, 581, A15

Tang M., Stark D., Chevallard J., Charlot S., 2019, MNRAS, 489, 2572

Tayal S. S., 2007, ApJS, 171, 331

Tayal S. S., Zatsarinny O., 2010, ApJS, 188, 32

Thuan T. X., Izotov Y. I., 2005, ApJS, 161, 240

Topping M. W., Shapley A. E., Reddy N. A., Sanders R. L., Coil A. L., Kriek M., Mobasher B., Siana B., 2020, MNRAS, 495, 4430

Vincenzo F., Belfiore F., Maiolino R., Matteucci F., Ventura P., 2016, MNRAS, 458, 3466

Watson D., Christensen L., Knudsen K. K., Richard J., Gallazzi A., Michalowski M. J., 2015, Nature, 519, 327

Yang H. et al., 2017, ApJ, 844, 171

APPENDIX A: XSHOOTER SPECTRA

Table A1. Emission line intensities and equivalent widths.

					Galaxy					
	J0901+2119		J0925+1403		J1011+1947		J1154+2443		J1442−0209	
Ion	I(λ)/I(Hβ)[a]	EW[b]	I(λ)/I(Hβ)[a]	EW[b]	I(λ)/I(Hβ)[a]	EW[b]	I(λ)/I(Hβ)[a]	EW[b]	I(λ)/I(Hβ)[a]	EW[b]
2613 Fe II*	1.18 ± 0.27	0.8	1.11 ± 0.21	0.4	...	...	...	...	1.90 ± 0.49	0.7
2626 Fe II*	0.74 ± 0.19	0.5	1.56 ± 0.22	0.5	...	...	...	...	2.17 ± 0.10	0.8
2796 Mg II	14.88 ± 0.82	10.7	14.35 ± 0.86	6.1	6.08 ± 0.48	5.0	12.48 ± 0.97	6.1	24.57 ± 1.33	11.9
2803 Mg II	7.61 ± 0.61	5.7	7.15 ± 0.70	3.1	3.37 ± 0.38	2.8	6.66 ± 0.89	3.3	12.91 ± 1.01	6.4
3188 He I	3.28 ± 0.19	3.0	3.31 ± 0.27	1.9	2.54 ± 0.35	2.4	3.29 ± 0.31	2.0	3.67 ± 0.29	2.1
3322 [Fe II]	0.37 ± 0.10	0.4	...	...	...	...	...	...	...	...
3692 H18	0.50 ± 0.09	0.8	0.69 ± 0.15	0.6	0.79 ± 0.12	1.5	0.98 ± 0.15	1.1	1.54 ± 0.27	1.4
3697 H17	0.50 ± 0.10	0.7	1.17 ± 0.22	1.1	1.07 ± 0.11	2.0	1.29 ± 0.15	1.5	1.76 ± 0.31	1.7
3703 H16+O III	1.50 ± 0.15	2.6	1.96 ± 0.20	1.9	1.82 ± 0.14	3.4	1.32 ± 0.20	1.5	3.65 ± 0.82	1.4
3712 H15	3.54 ± 0.41	2.5	4.19 ± 0.62	1.2	3.08 ± 0.32	2.8	4.79 ± 0.64	2.2	1.79 ± 0.06	1.0
3722 H14	1.31 ± 0.10	0.9	0.48 ± 0.08	0.2	14.98 ± 0.50	29.7	2.90 ± 0.25	2.8	...	...
3727 [O II]	90.12 ± 2.88	192.8	109.81 ± 3.53	121.8	28.66 ± 0.94	57.9	49.33 ± 1.67	56.4	94.27 ± 3.04	92.7
3734 H13	1.83 ± 0.12	2.8	2.22 ± 0.18	2.0	2.18 ± 0.21	3.5	2.47 ± 0.24	2.8	2.84 ± 0.25	2.8
3750 H12	5.18 ± 0.26	7.6	5.20 ± 0.45	2.5	4.06 ± 0.26	5.6	5.29 ± 0.75	3.0	5.66 ± 0.45	3.3
3771 H11	5.97 ± 0.28	8.1	6.31 ± 0.38	3.4	5.05 ± 0.30	6.4	6.91 ± 0.61	4.8	6.20 ± 0.49	3.9
3798 H10	6.66 ± 0.28	8.4	7.74 ± 0.37	5.4	5.47 ± 0.30	7.4	7.94 ± 0.59	5.8	7.14 ± 0.43	4.3
3820 He I	1.40 ± 0.09	2.7	0.71 ± 0.10	0.7	1.22 ± 0.11	2.8	...	...	0.93 ± 0.09	0.9
3835 H9	9.18 ± 0.34	14.5	9.43 ± 0.41	6.6	7.39 ± 0.36	13.2	10.25 ± 0.53	7.9	9.87 ± 0.45	7.1
3869 [Ne III]	55.21 ± 1.74	98.7	49.90 ± 1.60	50.2	48.92 ± 1.58	83.3	42.18 ± 1.38	44.5	53.81 ± 1.72	52.5
3889 He I + H8	20.54 ± 0.67	38.7	21.59 ± 0.74	19.0	15.42 ± 0.56	23.2	22.24 ± 0.80	22.0	21.83 ± 0.77	17.7
3968 [Ne III] + H7	17.55 ± 0.58	36.8	14.59 ± 0.51	13.2	13.55 ± 0.45	34.6	16.92 ± 0.65	18.2	18.15 ± 0.65	19.0
4026 He I	1.46 ± 0.08	2.8	1.66 ± 0.13	1.8	1.38 ± 0.12	3.1	...	...	2.43 ± 0.23	2.9
4069 [S II]	1.10 ± 0.07	2.2	1.03 ± 0.10	1.2	0.46 ± 0.06	1.1	...	...	1.11 ± 0.17	1.2
4076 [S II]	0.50 ± 0.05	1.1	0.53 ± 0.07	0.6	0.20 ± 0.03	0.5	...	...	0.45 ± 0.53	0.5
4101 Hδ	28.53 ± 0.88	61.2	28.64 ± 0.91	30.2	24.00 ± 0.80	47.5	26.21 ± 1.13	37.4	27.93 ± 0.91	29.0
4340 Hγ	46.06 ± 1.40	103.8	46.69 ± 1.44	63.5	47.90 ± 1.49	178.6	45.56 ± 1.58	64.2	47.01 ± 1.49	61.4
4363 [O III]	10.81 ± 0.37	26.3	7.23 ± 0.31	11.1	16.38 ± 0.56	35.4	13.43 ± 0.76	24.5	10.63 ± 0.43	14.8
4471 He I	4.08 ± 0.23	12.7	4.07 ± 0.24	6.4	3.27 ± 0.31	8.4	3.95 ± 0.52	7.9	3.56 ± 0.31	5.2
4658 [Fe III]	0.73 ± 0.13	2.2	1.12 ± 0.13	1.9	...	...	...	...	...	...
4686 He II	0.88 ± 0.18	2.7	1.13 ± 0.16	1.9	1.78 ± 0.25	5.3	2.02 ± 0.45	4.7	0.99 ± 0.13	1.4
4713 [Ar IV] + He I	2.52 ± 0.19	9.0	1.49 ± 0.26	2.8	2.91 ± 0.16	7.5	2.66 ± 0.35	6.6	1.03 ± 0.16	1.6
4740 [Ar IV]	1.14 ± 0.24	3.9	0.86 ± 0.20	1.6	2.27 ± 0.18	6.6	2.82 ± 0.37	9.5	0.77 ± 0.16	1.4
4861 Hβ	100.00 ± 2.88	357.5	100.00 ± 2.91	208.1	100.00 ± 2.89	314.9	100.00 ± 2.99	255.1	100.00 ± 2.91	186.8
4922 He I	0.89 ± 0.14	3.1	0.76 ± 0.12	1.5	1.42 ± 0.11	4.8	...	...	0.99 ± 0.15	1.9
4959 [O III]	232.94 ± 6.70	833.9	198.62 ± 5.76	387.4	278.38 ± 8.02	774.7	188.89 ± 5.55	356.6	209.38 ± 6.08	358.1
4986 [Fe III]	0.83 ± 0.10	2.6	0.54 ± 0.07	1.2	...	...	...	...	...	...
5007 [O III]	694.26 ± 19.96	2229.0	592.10 ± 17.13	1317.0	826.75 ± 23.83	1848.0	573.15 ± 17.05	720.5	643.46 ± 18.61	1097.0
5016 He I	1.18 ± 0.06	2.4	1.28 ± 0.11	1.8	...	...	...	...	1.34 ± 0.10	1.3
5041 Si II	0.27 ± 0.08	1.0	...	...	...	...	...	...	0.53 ± 0.08	1.0
5048 He I	0.27 ± 0.07	1.1	...	...	...	...	...	...	...	...
5056 Si II	0.46 ± 0.07	1.9	...	...	...	...	...	...	...	...
5755 [N II]	0.43 ± 0.08	2.4	...	...	...	...	...	...	...	...

Table A1 *– continued*

| | Galaxy | | | | | | | | | |
| | J0901+2119 | | J0925+1403 | | J1011+1947 | | J1154+2443 | | J1442−0209 | |
Ion	$I(\lambda)/I(\mathrm{H}\beta)^a$	EW^b	$I(\lambda)/I(\mathrm{H}\beta)^a$	EW^b	$I(\lambda)/I(\mathrm{H}\beta)^a$	EW^b	$I(\lambda)/I(\mathrm{H}\beta)^a$	EW^b	$I(\lambda)/I(\mathrm{H}\beta)^a$	EW^b
5876 He I	11.25 ± 0.38	55.9	10.91 ± 0.36	33.1	12.39 ± 0.39	60.5	11.46 ± 0.43	53.0	10.24 ± 0.73	35.7
6300 [O I]	2.65 ± 0.11	15.6	3.07 ± 0.12	11.9	1.73 ± 0.14	11.1	2.13 ± 0.20	10.2	2.99 ± 0.13	11.0
6312 [S III]	1.31 ± 0.08	8.2	1.27 ± 0.09	5.1	0.97 ± 0.11	6.7	1.12 ± 0.17	5.1	1.29 ± 0.08	4.5
6364 [O I]	0.94 ± 0.06	5.5	1.02 ± 0.09	4.1	0.59 ± 0.08	5.0	1.09 ± 0.20	5.8	1.00 ± 0.09	3.7
6548 [N II]	3.12 ± 0.12	15.1	2.45 ± 0.12	4.6	1.54 ± 0.14	8.4	1.77 ± 0.31	8.9	1.66 ± 0.10	4.0
6563 Hα	283.65 ± 8.82	1902.0	285.04 ± 8.92	1105.0	281.09 ± 8.77	2503.0	277.61 ± 8.82	1361.0	282.85 ± 8.85	1086.0
6583 [N II]	11.83 ± 0.38	75.2	11.77 ± 0.38	46.8	3.95 ± 0.18	21.5	4.90 ± 0.27	22.1	8.42 ± 0.29	31.9
6678 He I	3.43 ± 0.13	28.4	3.08 ± 0.12	13.5	3.35 ± 0.13	25.5	3.46 ± 0.20	19.2	2.93 ± 0.12	13.6
6716 [S II]	7.74 ± 0.26	53.0	9.40 ± 0.31	43.9	2.39 ± 0.10	15.5	4.57 ± 0.24	19.5	8.68 ± 0.30	34.2
6731 [S II]	6.90 ± 0.23	40.5	7.77 ± 0.27	34.3	2.36 ± 0.10	16.5	3.64 ± 0.27	14.3	6.51 ± 0.23	25.6
7065 He I	5.01 ± 0.18	36.2	4.15 ± 0.17	18.8	5.58 ± 0.22	36.3	4.45 ± 0.44	35.5	4.14 ± 0.17	20.2
7136 [Ar III]	5.92 ± 0.23	47.9	5.67 ± 0.23	28.0	3.40 ± 0.15	36.3	3.53 ± 0.48	19.3	5.02 ± 0.21	22.9
7320 [O II]	2.02 ± 0.11	16.6	2.11 ± 0.13	11.8	...	...	...	...	1.53 ± 0.10	5.8
7330 [O II]	1.41 ± 0.12	11.7	1.75 ± 0.13	9.8	...	...	...	...	1.51 ± 0.14	6.0
8750 P12	...	...	...	...	...	...	...	...	1.71 ± 0.24	17.1
8863 P11	...	...	...	...	...	...	...	...	1.64 ± 0.18	15.0
9015 P10	...	...	1.27 ± 0.12	26.6	...	...	...	...	...	...
9069 [S III]	7.25 ± 0.31	210.0	9.06 ± 0.39	205.4	8.24 ± 0.42	68.6	10.99 ± 1.11	146.7	9.47 ± 0.49	36.7
9229 P9	1.95 ± 0.12	35.4	1.35 ± 0.11	19.1	2.62 ± 0.22	19.1	2.15 ± 0.20	...	2.15 ± 0.20	14.8
9531 [S III]	16.85 ± 0.65	797.7	19.91 ± 0.78	370.1	20.48 ± 0.84	223.3	32.57 ± 1.52	169.6	28.87 ± 1.16	221.8
9546 P8	2.05 ± 0.11	98.2	1.76 ± 0.10	24.9	4.02 ± 0.24	60.8	6.88 ± 0.66	140.6	4.06 ± 0.23	37.0
10049 P7	3.08 ± 0.14	124.6	2.95 ± 0.15	62.7	5.56 ± 0.30	90.2	...	...	5.10 ± 0.28	41.3
10829 He I	14.42 ± 0.60	984.7	5.21 ± 0.29	167.0	54.84 ± 2.20	1051.0	55.27 ± 2.50	122.3	36.23 ± 1.53	119.1
10941 Pγ	3.88 ± 0.21	193.9	0.98 ± 0.10	23.9	8.54 ± 0.40	239.5	13.98 ± 1.56	828.0	9.14 ± 0.48	216.5
12570 [Fe II]	0.47 ± 0.03	24.6	...	14.6	...	...	...	...	1.25 ± 0.10	21.2
12790 He I	0.44 ± 0.04	32.3	0.41 ± 0.05		...	...	...	...	...	...
12821 Pβ	7.12 ± 0.30	432.5	7.56 ± 0.32	282.1	13.28 ± 0.56	455.1	16.42 ± 0.96	319.4	17.13 ± 0.73	257.8
16430 [Fe II]	0.25 ± 0.02	61.8	...	...	...	...	...	...	...	...
18756 Pα	10.64 ± 0.58	1816.0	20.96 ± 1.03	347.0	...	...	...	...	...	...
EW(abs)^c	3.59		2.81		3.30		3.39		2.47	
C(Hβ)^d	0.180		0.145		0.155		0.020		0.170	
F(Hβ)^e	11.78		21.61		13.12		9.77		19.44	

^{a}Ratio of extinction corrected fluxes to Hβ multiplied by 100.
^{b}Equivalent widths of emission lines in Å.
^{c}Equivalent widths of underlying hydrogen absorption lines in Å.
^{d}Extinction coefficient, obtained from Balmer decrement.
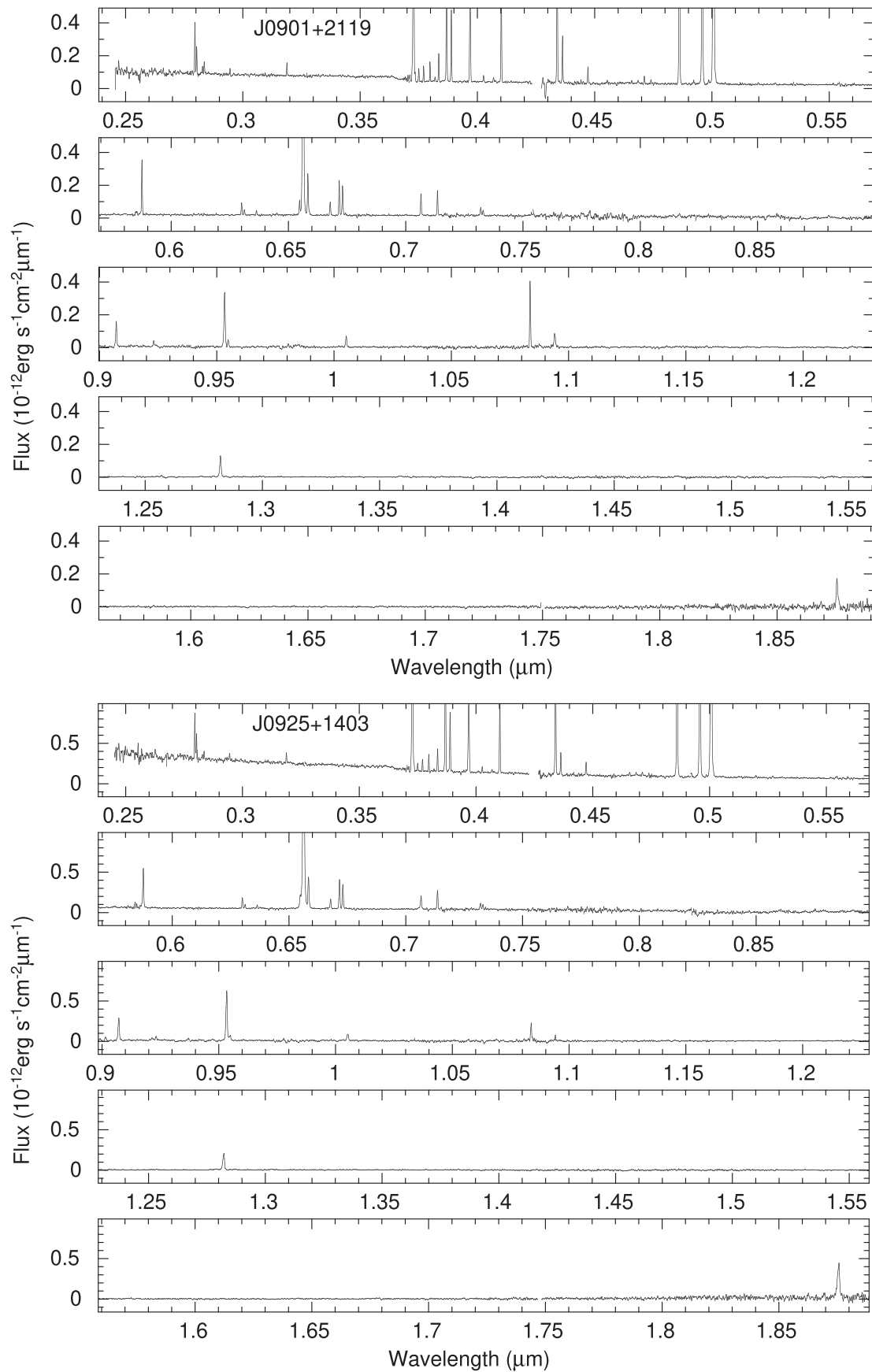^{e}Observed flux in units of 10^{-16} erg s^{-1} cm^{-2}.
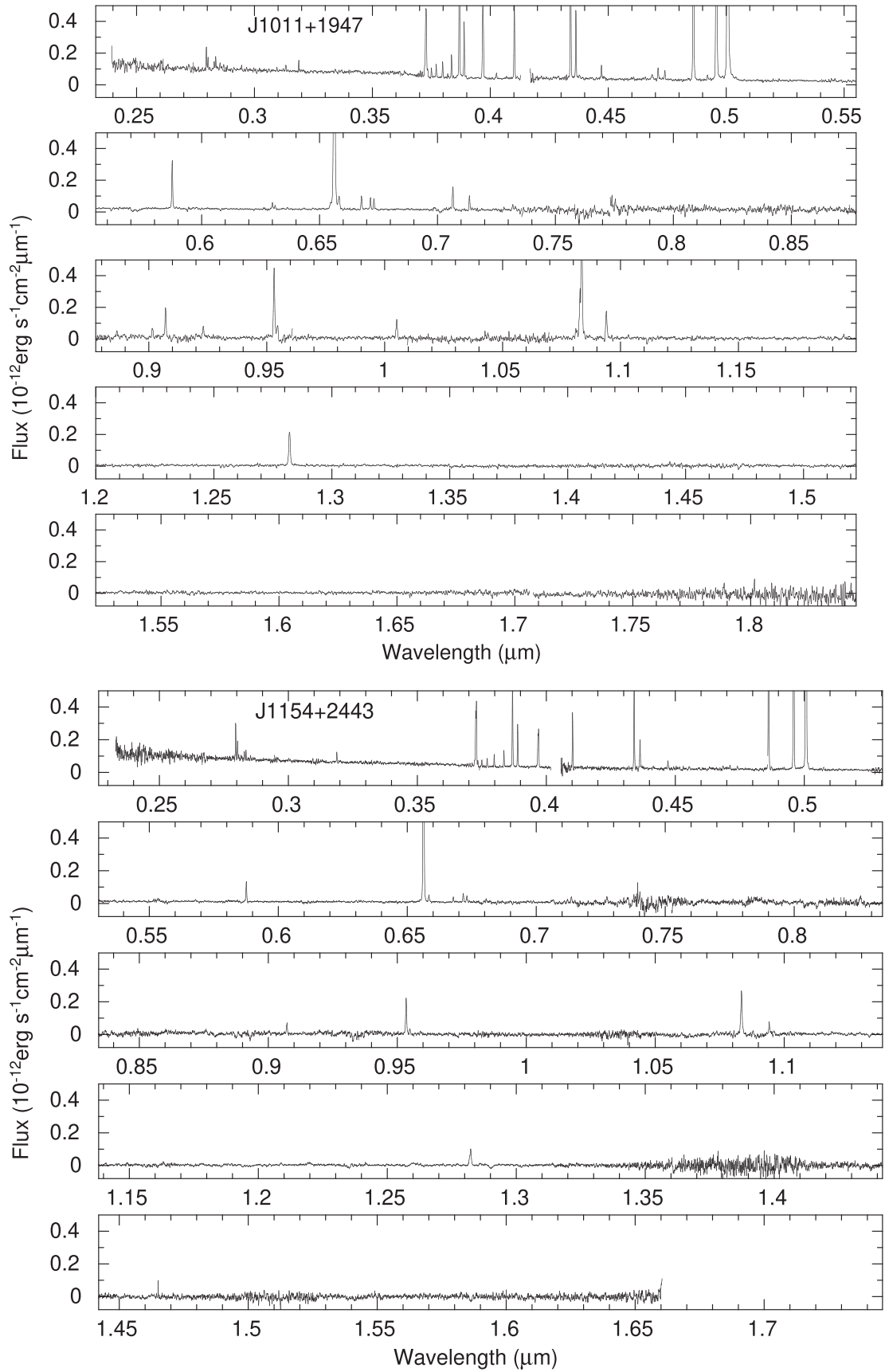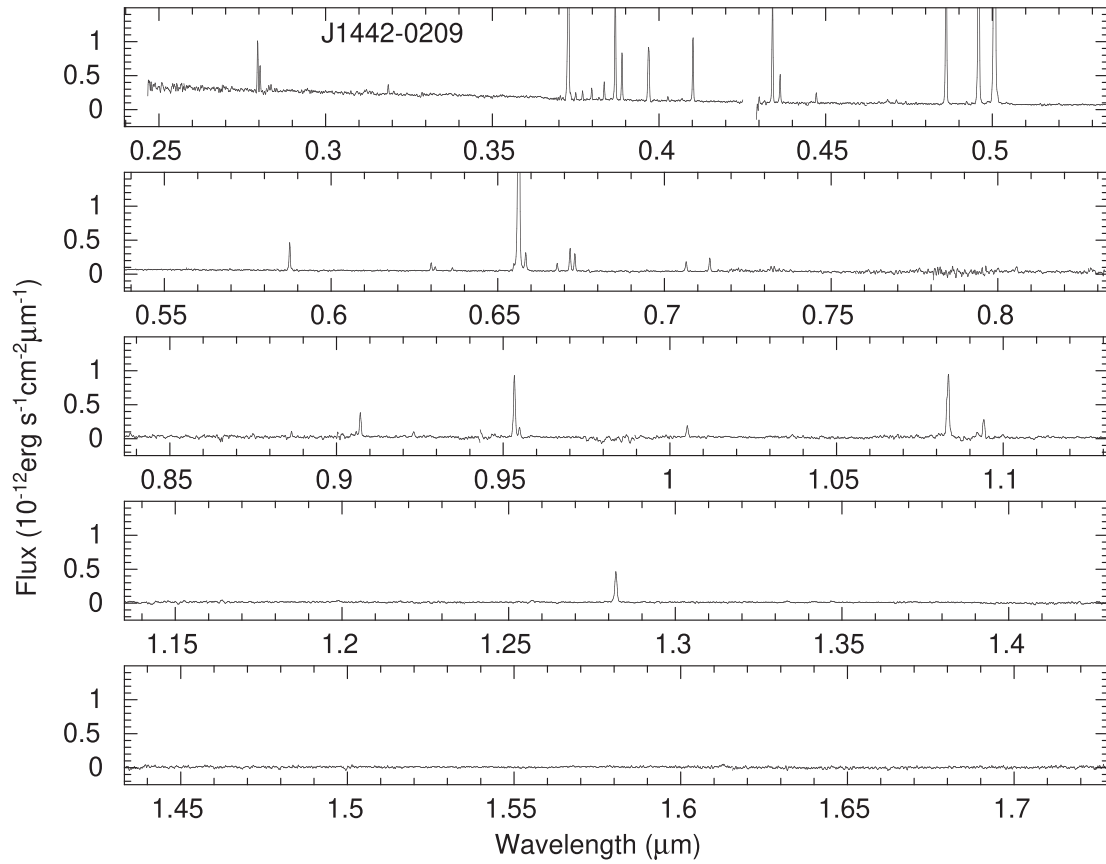
Figure A1. Rest-frame XShooter spectra.

Figure A1 – *continued*

Figure A1 *– continued*

This paper has been typeset from a TEX/LATEX file prepared by the author.